



## Repeated megafloods from glacial Lake Vitim, Siberia, to the Arctic Ocean over the past 60,000 years

Martin Margold <sup>a,\*</sup>, John D. Jansen <sup>b</sup>, Alexandru T. Codilean <sup>c</sup>, Frank Preusser <sup>d</sup>, Artem L. Gurinov <sup>e</sup>, Toshiyuki Fujioka <sup>f</sup>, David Fink <sup>f</sup>

<sup>a</sup> Department of Physical Geography, Stockholm University, SE-10691, Stockholm, Sweden

<sup>b</sup> Department of Geoscience, Aarhus University, Høegh-Guldbergs Gade 2, 8000, Aarhus, Denmark

<sup>c</sup> School of Earth & Environmental Sciences, University of Wollongong, Northfields Avenue, Wollongong, NSW, 2522, Australia

<sup>d</sup> Institute of Earth and Environmental Sciences, Albert-Ludwigs-Universität Freiburg, Albertstr. 23-B, 79104, Freiburg, Germany

<sup>e</sup> Department of Geomorphology & Palaeogeography, Faculty of Geography, Lomonosov Moscow State University, Leninskoe Gory, GSP-1, Moscow, 119991, Russian Federation

<sup>f</sup> Australian Nuclear Science & Technology Organisation, New Illawarra Road, Lucas Heights, NSW, 2234, Australia



### ARTICLE INFO

#### Article history:

Received 13 October 2017

Received in revised form

22 January 2018

Accepted 5 March 2018

Available online 20 March 2018

### ABSTRACT

Cataclysmic outburst floods transformed landscapes and caused abrupt climate change during the last deglaciation. Whether such events have also characterized previous deglaciations is not known. Arctic marine cores hint at megafloods prior to Oxygen Isotope Stage (OIS) 2, but the overprint of successive glaciations means that geomorphological traces of ancient floods remain scarce in Eurasia and North America. Here we present the first well-constrained terrestrial megaflood record to be linked with Arctic archives. Based on cosmogenic-nuclide exposure dating and optically stimulated luminescence dating applied to glacial-lake sediments, a 300-m deep bedrock spillway, and giant eddy-bars > 200-m high, we reconstruct a history of cataclysmic outburst floods from glacial Lake Vitim, Siberia, to the Arctic Ocean over the past 60,000-years. Three megafloods have reflected the rhythm of Eurasian glaciations, leaving traces that stretch more than 3500 km to the Lena Delta. The first flood was coincident with deglaciation from OIS-4 and the largest meltwater spike in Arctic marine-cores within the past 100,000 years (isotope-event 3.31 at 55.5 ka). The second flood marked the lead up to the local Last Glacial Maximum, and the third flood occurred during the last deglaciation. This final 3000 km<sup>3</sup> megaflood stands as one of the largest freshwater floods ever documented, with peak discharge of 4.0–6.5 million m<sup>3</sup>s<sup>-1</sup>, mean flow depths of 120–150 m, and average flow velocities up to 21 m s<sup>-1</sup>.

© 2018 Elsevier Ltd. All rights reserved.

### 1. Introduction

Discoveries of cataclysmic glacial lake outburst floods have expanded the scale and frequency of known mass-transport events on Earth and other planets (Baker, 2001). Freshwater discharges from glacial lakes associated with waning ice sheets are thought to have disrupted ocean circulation and sparked pronounced climate fluctuations (Broecker et al., 1989; Barber et al., 1999) while transporting cubic kilometres of rock, soil, and biomass (Korup and Tweed, 2007). During the last deglaciation in North America, the final collapse of glacial Lake Agassiz-Ojibway triggered the 8.2 ka

cold event (Barber et al., 1999), and outbursts from Lake Missoula cut the spectacular Channeled Scabland (Baker and Bunker, 1985; Baker et al., 2016). However, records of outbursts prior to Oxygen Isotope Stage 2 (OIS-2) have remained elusive in both Eurasia and North America (e.g., Bjornstad et al., 2001), even though Arctic marine cores show that large Eurasian glacial lakes (Fig. 1; Mangerud et al., 2004; Svendsen et al., 2004) were a major meltwater source (Spielhagen et al., 2004).

#### 1.1. Pleistocene glacial lake outburst floods in southern Siberia

Floods from glacial lakes dammed by the continental sectors of the Eurasian Ice Sheet are yet to be reconstructed in detail (see Mangerud et al., 2004; Komatsu et al., 2016), but more information is available on outbursts from glacial lakes in southern Siberia.

\* Corresponding author.

E-mail address: [martin.margold@natgeo.su.se](mailto:martin.margold@natgeo.su.se) (M. Margold).

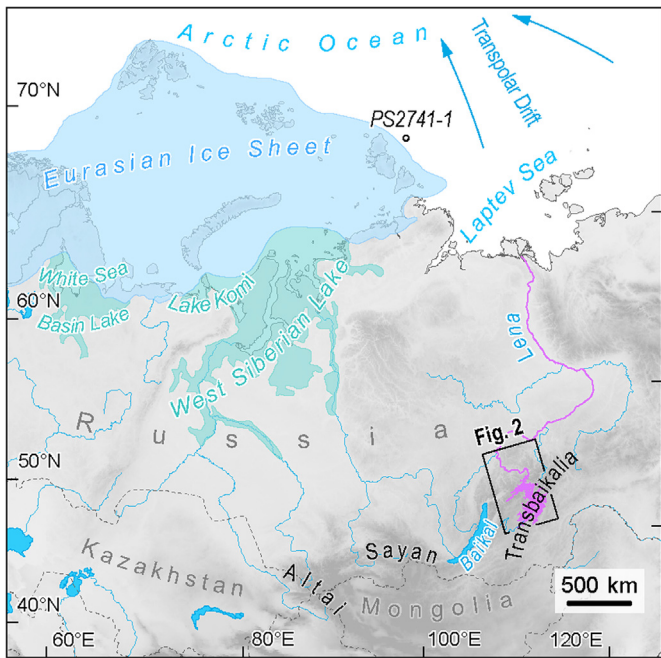


**Fig. 1. Regional setting.** Glacial Lake Vitim and the flood route to the Arctic Ocean along the Vitim and Lena rivers are drawn in magenta, glacial lakes dammed by the Eurasian Ice Sheet during OIS-4 (Mangerud et al., 2004) are in green. The study area of Transbaikalia and the location of Fig. 2 are marked in black, as well as the Altai and Sayan mountain ranges discussed in the text. (For interpretation of the references to colour in this figure legend, the reader is referred to the Web version of this article.)

Here, extensive mountain ranges with alpine relief surround deep intermontane basins (Petit and Déverchère, 2006; Krivonogov and Safonova, 2017) that have hosted large glacial lakes repeatedly in the Pleistocene when their drainage became blocked by glaciers (Grosswald and Rudoy, 1996; Komatsu et al., 2016). The elevated positions of these basins within the continental interior meant that sudden failure of the ice dams unleashed high-magnitude floods down the valleys of the major Siberian rivers towards the Arctic Ocean (Grosswald and Rudoy, 1996; Carling et al., 2010; Komatsu et al., 2016). The floods from basins in the Altai and Sayan mountains (Fig. 1) have received considerable attention (e.g., Baker et al., 1993; Herget, 2005; Reuther et al., 2006; Komatsu et al., 2009; Bohorquez et al., 2016; Batbaatar and Gillespie, 2016a,b): the Lake Chuja-Kuray floods are the only outbursts comparable in discharge to the Missoula floods (O'Connor and Costa, 2004) that have been reconstructed in detail. In comparison, the Pleistocene glacial lakes and floods of Transbaikalia (Fig. 1) have thus far attracted little interest. Building on earlier reconnaissance work (Margold and Jansson, 2011; Margold et al., 2011), here we reconstruct outburst floods of cataclysmic magnitude from glacial Lake Vitim (Figs. 1 and 2), based on their erosional and depositional legacy stretching from the headwaters of the Vitim River down to the Lena River delta and Arctic Ocean sediment cores.

## 2. Glacial Lake Vitim

The Vitim River, one of the largest tributaries of the Lena, has its source in the mountains east of Lake Baikal. After crossing the Vitim Plateau in its upper reaches, the Vitim drains the Muya-Kuanda Depression (Fig. 2), a deep intermontane basin containing >1 km depth of sediments associated with the north-east arm of the Baikal Rift System (Petit and Déverchère, 2006; Enikeev, 2008; Krivonogov and Safonova, 2017). North of the Muya-Kuanda

Depression, the Vitim cuts a narrow valley between the North Muya and Kodar ranges, which are mostly composed of the crystalline rocks of the Baikal–Muya Orogen (Rytsk et al., 2011), reaching elevations of ~3000 m above sea level. The Vitim then crosses the Baikal–Patom Uplands before meeting the Lena at the north-western front of the uplands (Fig. 2).

The existence of an ice-dammed lake in the Muya-Kuanda Depression was first suggested by Obruchev (1929) and was briefly noted by Grosswald and Rudoy (1996). While the origin of the palaeo-lake (Fig. 2) was disputed at first (cf. Kulchitskiy and Pulyavskiy, 1988; Kulchitskiy et al., 1995; Ufimtsev et al., 1998; Kolomiets, 2008), the damming of the Vitim River by Pleistocene glaciers from the Kodar Mountains is now accepted as the primary forming mechanism (Osadchiy, 1979, 1982; Bazarov, 1986; Krivonogov and Takahara, 2003; Enikeev, 2009; Margold and Jansson, 2011; Margold et al., 2011). Margold et al. (2016) established that glaciers were sufficiently extensive to dam the Vitim River most recently during the Last Glacial Maximum at OIS-2 (Fig. 2). The geomorphological record of glacial Lake Vitim (Fig. 2) was mapped by Margold and Jansson (2011) using Landsat imagery, Shuttle Radar Topographic Mission (SRTM) 3 arc-sec data, and Google Earth. A relict shoreline was traced along a substantial portion of the lake's perimeter at a constant 840 m above sea level (Fig. 2; Kulchitskiy and Pulyavskiy, 1988; Margold et al., 2011). This elevation matches an overflow to the Amur River, which drains to the Pacific Ocean, and so marks the maximum possible lake level at which the lake covered an area of 23,500 km<sup>2</sup> (Fig. 2; Margold et al., 2011). The lake volume was calculated at 3000 km<sup>3</sup> using the 3 arc-sec SRTM data (Margold et al., 2011), and based on present-day river discharge data for the Vitim River in the Muya-Kuanda Depression, it was estimated that lake-filling would take <100 years to reach the maximum impoundment depth of 490 m (Fig. 2; Margold et al., 2011). In their GIS analysis, Margold et al. (2011) identified geomorphological evidence for a catastrophic release of the lake: a 6 km long, 2 km wide, and 300 m deep bedrock spillway in the ice dam area ~15 km downstream from Lake Oron (Figs. 3 and 4). In addition, the Vitim valley-sides appear to have been trimmed by large-magnitude floods immediately downstream of Lake Oron (Margold et al., 2011, Fig. 3). Yet there has thus far been no attempt to reconstruct the outburst floods from glacial Lake Vitim based on evidence from the field and the first such effort is reported here.

## 3. Methods

### 3.1. Remote sensing and field surveys

We refine the geomorphology mapped by Margold and Jansson (2011) with a resurvey of the Vitim valley at higher resolution thanks to the release of SRTM 1 arc-sec data in 2014. Mapping was carried out with ArcGIS 10.2 (Environmental Systems Research Institute, 2011). Two field expeditions (summer 2011 and 2012) aimed to verify the mapping and to search for additional information about the lake and its cataclysmic drainage. The fieldwork focused on two areas: (i) the former lake basin (the Muya-Kuanda Depression), and (ii) the ice dam area and the Vitim valley downstream.

Relict shorelines were visited at two sites in the Muya-Kuanda Depression, but no dateable materials were located. A well-rounded boulder interpreted as an ice rafted dropstone was found on the slope below one of the shorelines (56.431018° N, 115.467247° E), indicating that glaciers were calving into Lake Vitim, consistent with earlier mapping (Margold and Jansson, 2011). Travelling by boat along the Muya River (Fig. 2) led to the discovery of glaciolacustrine sediments exposed in the river bank (Fig. 5). Despite two attempts in 2011 and 2012, we were not able to

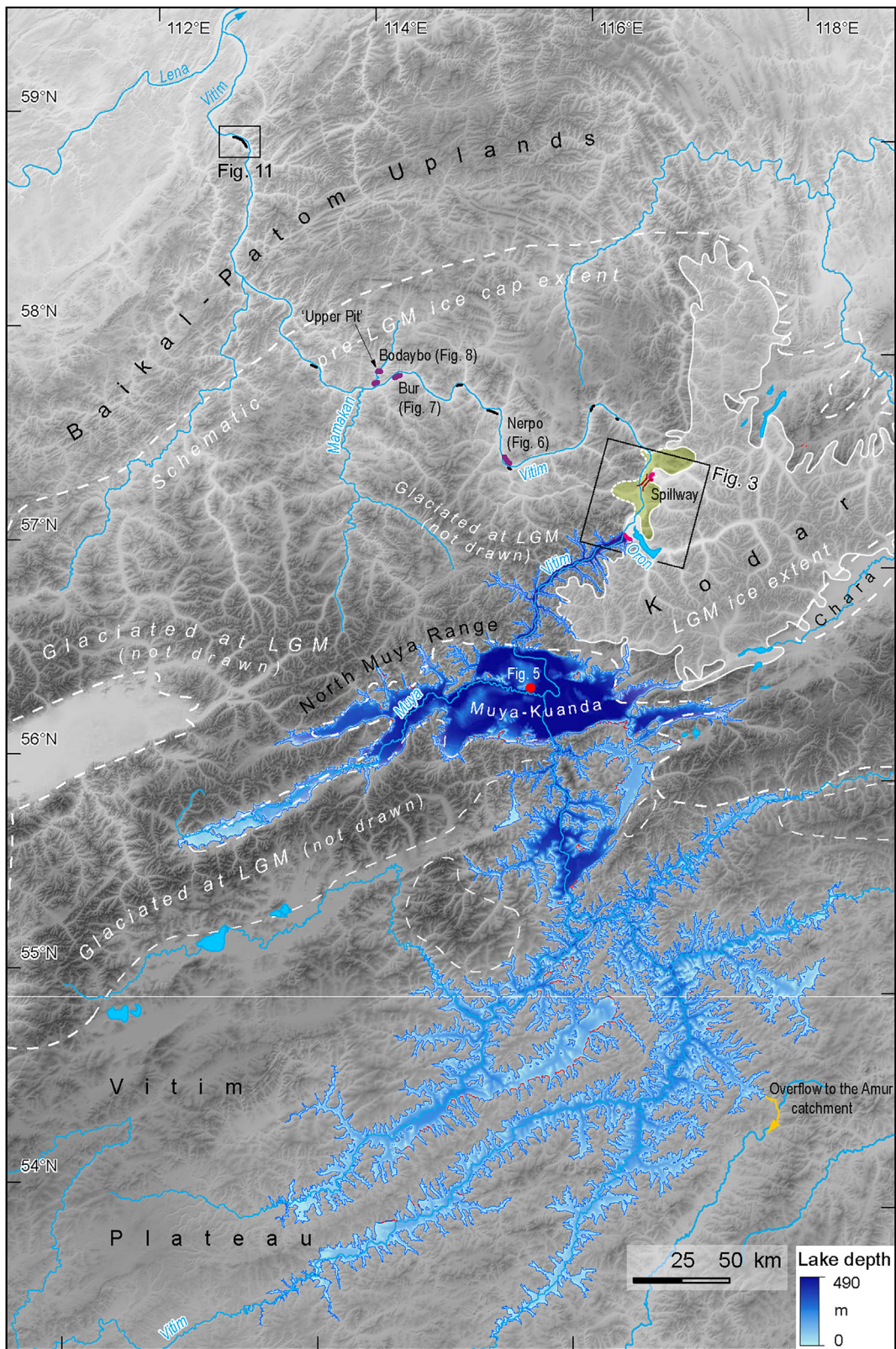


**Fig. 2. Glacial Lake Vitim and the surrounding region.** Reconstructed minimum LGM ice extent in the Kodar Mountains is drawn in white shading; a more extensive glaciation indicated by the glacial geomorphology is shown schematically (white dashes; Margold et al., 2016). Also shown: ice-dam area (green), Muya River glaciolacustrine section (red dot), dated moraines at Oron and spillway (pink), giant bars dated (purple) and undated (black), relict shorelines (red), and overflow to the River Nercha-Amur (yellow). (For interpretation of the references to colour in this figure legend, the reader is referred to the Web version of this article.)

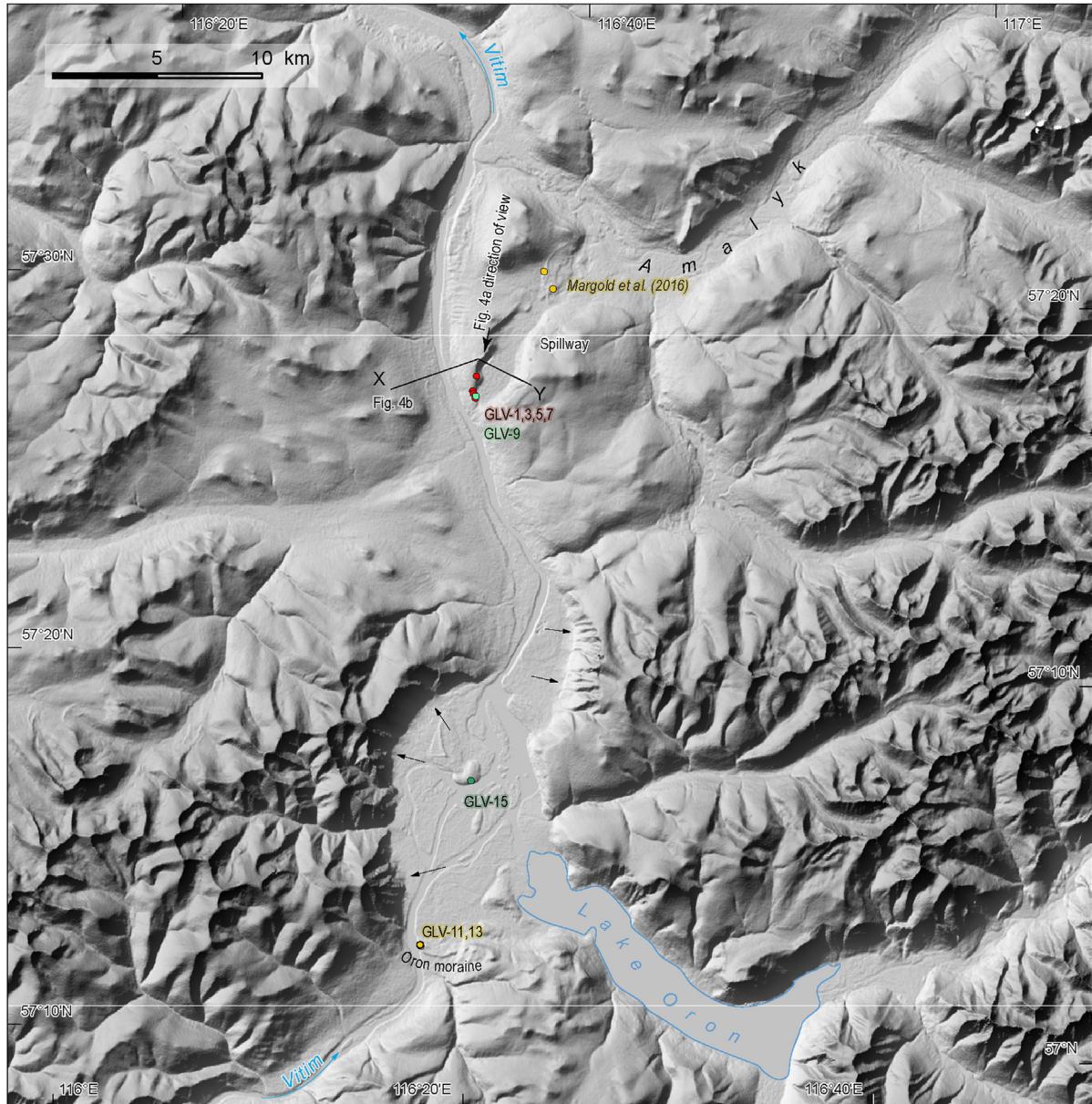


**Fig. 3. Glacial Lake Vitim ice dam area.** DEM-derived hill-shaded image (SRTM 1 arc-sec data), including glacially modified, interconnected valleys surrounding the spillway. Also shown: location of  $^{10}\text{Be}$  exposure dating samples taken from the spillway rim (red dots), spillway talus slope (light green dot), and a talus block on a bedrock island within Oron delta (dark green dot);  $^{10}\text{Be}$ -dated moraine boulders (yellow); and flood-trimmed slopes of the Vitim valley (black arrows) downstream of Lake Oron. Note view direction and transect location for Fig. 4a and b. (For interpretation of the references to colour in this figure legend, the reader is referred to the Web version of this article.)

locate and re-examine a Muya riverbank exposure described by Russian authors (Kulchitskiy et al., 1990; Krivonogov and Takahara, 2003) as comprising two glaciolacustrine units separated by a palaeosol  $^{14}\text{C}$ -dated to ~45–37 ka. Other sedimentary exposures were visited elsewhere in the Muya-Kuanda Depression to gain an insight to the nature of sedimentation, reworking and erosion, as described in Section 4.4. A giant eddy bar, located across the Vitim River from the former settlement of Nerpo (Figs. 2 and 6), was discovered when boating down the Vitim. Other giant eddy bars at Bur (Figs. 2 and 7) and on a tributary, Bodaybo River (Figs. 2 and 8), were located thanks to sand extraction activities.

### 3.2. Geochronology

In order to establish a chronology for the existence of glacial

Lake Vitim and for its outburst events, we apply both optically stimulated luminescence (OSL) and cosmogenic nuclide exposure dating to depositional and erosional landforms associated with the floods. Namely, these are: the section with exposed glaciolacustrine sediments at the Muya River, the bedrock-incised spillway and the giant eddy bars at Nerpo, Bur, and Bodaybo. The location of these sites is marked in Fig. 2, the geomorphology of the ice-dam area with the location of the samples for  $^{10}\text{Be}$  surface exposure dating is displayed in Fig. 3, and the sedimentary stratigraphy at the sites from which we collected samples for OSL and for  $^{10}\text{Be}$  sediment depth-profiles is displayed in Figs. 5–8.

#### 3.2.1. Optically stimulated luminescence dating

All OSL samples were collected by hammering stainless steel tubes ( $30 \times 8$  cm) into freshly cut excavations. At the Muya River

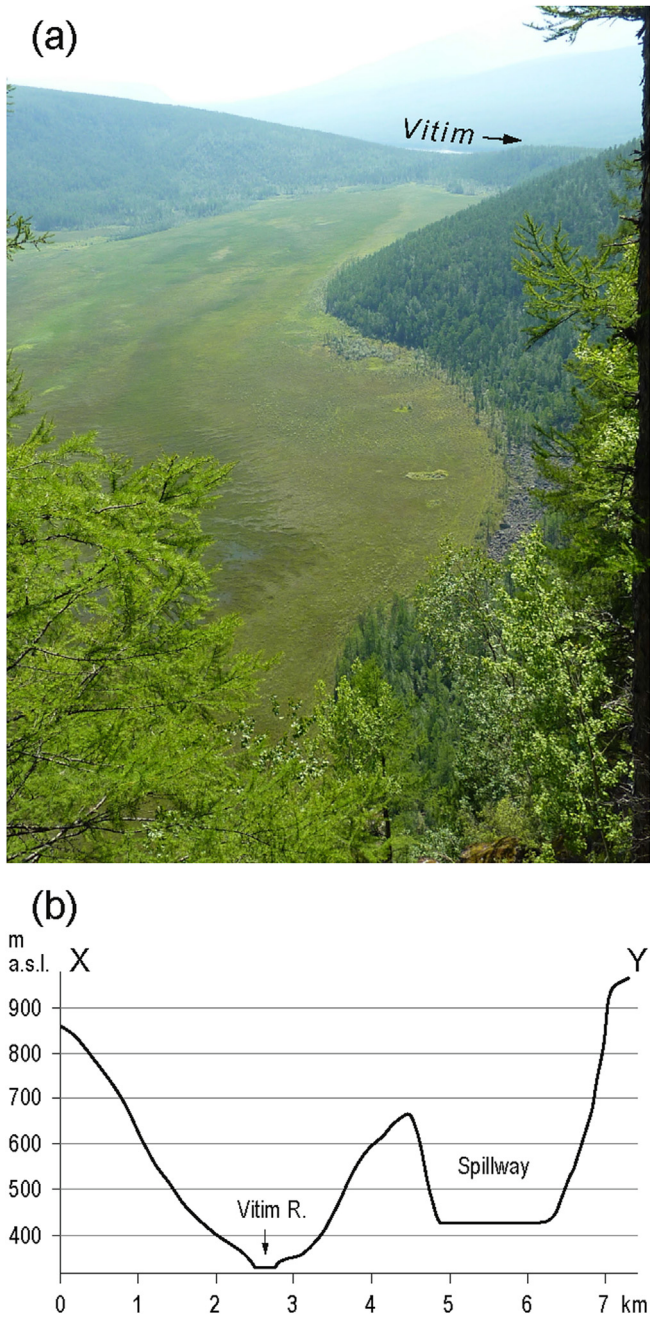


**Fig. 4. Spillway and Vitim valley transect.** (a) View from the south-west rim of the spillway (see Fig. 3 for the direction of view). Note the Vitim River visible in the distance. (b) Vitim valley and the spillway transect measured via SRTM 1-arc-sec data (see Fig. 3 for location).

sedimentary section (Figs. 2 and 5) a total of eight OSL samples were collected from fluvial sands and glaciolacustrine muds (samples GLV-11-1, GLV-11-3, MS-12-01 to MS-12-06; Table 1), although only three of these were measured successfully (Table 1). OSL samples were also collected from hand-excavated pits at the crest of the giant eddy bars at Nerpo (NT-12-01) and Bur (GLV-11-9; Figs. 2, 6 and 7, Table 1). A total of three OSL samples (GLV-11-5, GLV-11-7, BUP-12-01; Table 1) were collected from a sand extraction pit (the 'Upper Pit' site) cut into a giant eddy-bar in the Bodaybo River valley, a major tributary of the Vitim River (Figs. 2 and 8). Two samples were collected from the eddy bar sediments (GLV-11-5, GLV-11-7), and one sample was collected from the overlying thin

aeolian sand sheet (BUP-12-01; Fig. 8).

Samples were prepared and measured at the Stockholm University luminescence laboratory. Sediment from the outer parts from the tube was used for gamma spectrometric measurements (Preusser and Kasper, 2001). Cosmic dose was calculated using present-day depth. The average sediment moisture during burial was estimated based on present day water content and grain size composition of the sample. For two samples (GLV-11-1, GLV-11-3), we expect a significant change of sediment moisture in the past (due to submergence by Lake Vitim) and used  $20 \pm 5\%$  from burial until 10 ka ago, and  $8 \pm 4\%$  for the remaining time.

Material from the inner part of the sample was sieved (125–160  $\mu\text{m}$ ) and chemically pre-treated (HCl,  $\text{H}_2\text{O}_2$ , Na-oxalate). The quartz fraction was isolated using heavy liquids and then etched with 40% HF (60 min), followed by 10% HCl treatment (>120 min) and re-sieving to remove feldspar remains. Equivalent dose ( $\text{De}$ ) was determined (Risø DA-20) using a modified version of the SAR-protocol of Murray and Wintle (2000), with preheating at 230 °C for 10 s prior to all OSL measurements (blue diode stimulation for 60 s at 125 °C, Hoya U340 detection filter). Measurements were also conducted on small aliquots (2 mm, ~100 grains), but these turned out to be problematic as discussed below.

### 3.2.2. Cosmogenic nuclide dating

All samples for  $^{10}\text{Be}$  dating of rock surfaces were collected with a hammer and chisel. Four bedrock samples (GLV-1, 3, 5, 7) were collected along the western rim of the spillway (Fig. 3) and a single sample (GLV-9, Fig. 9) from a talus block on the spillway slopes. Two boulders were sampled on the Oron moraine (GLV-11-13; Fig. 3; their ages were reported in Margold et al., [2016]) and one sample from a large detached block in a bedrock outcrop (GLV-15) in the Oron delta (Fig. 3). All of the collected samples were of granitic lithology with the exception of samples GLV-13 (mica schist) and GLV-15 (metasedimentary). Some of the sampled surfaces were covered by a moss blanket but none of them displayed signs of any substantial weathering. In addition, two  $^{10}\text{Be}$  sediment depth-profiles were collected; one at the crest of Nerpo giant eddy-bar (6 samples, Fig. 6) and the other at 'Upper Pit' on the Bodaybo River (11 samples, Fig. 8).

The GLV series of samples (Table 2), collected in 2011, were processed at the Deutsches GeoForschungsZentrum GFZ, Potsdam. Quartz was separated and cleaned following procedures based on Kohl and Nishiizumi (1992) and  $^{10}\text{Be}$  was extracted using ion chromatography following procedures described by von Blanckenburg et al. (1996).  $^{10}\text{Be}/^{9}\text{Be}$  ratios were measured at the University of Cologne's accelerator mass spectrometer (AMS) laboratory (Dewald et al., 2013). The  $^{10}\text{Be}/^{9}\text{Be}$  ratio of full procedural blanks, prepared from a phenakite Be spike solution added to all samples, was  $(0.8 \pm 0.3) \times 10^{-15}$  and blank corrected  $^{10}\text{Be}/^{9}\text{Be}$  ratios ranged between  $(158 \pm 6) \times 10^{-15}$  and  $(792 \pm 8) \times 10^{-15}$ .  $^{10}\text{Be}/^{9}\text{Be}$  ratios were normalised to the 2007 KNSTD standard KN01-5-3 with nominal  $^{10}\text{Be}/^{9}\text{Be}$  ratio of  $6.32 \times 10^{-12}$  (Nishiizumi et al., 2007). The Nerpo and Bodaybo depth-profile sediment samples (BUP and NT series, Table 3), collected in 2012, were processed at the Australian Nuclear Science and Technology Organisation (ANSTO) using an initial treatment of successive etching by hot phosphoric acid (Mifsud et al., 2013) and a final clean via standard HF/HNO<sub>3</sub> methods.  $^{10}\text{Be}$  was extracted using ion-chromatography methods reported in Child et al. (2000). Three full procedural blanks prepared from a similar phenakite spike solution gave a final mean  $^{10}\text{Be}/^{9}\text{Be}$  ratio of  $(3.5 \pm 0.4) \times 10^{-15}$  ( $n = 8$ , mean of 3 targets). Blank corrected  $^{10}\text{Be}/^{9}\text{Be}$  ratios ranged between  $(36 \pm 2) \times 10^{-15}$  and  $(533 \pm 9) \times 10^{-15}$ . The  $^{10}\text{Be}/^{9}\text{Be}$  ratios were measured at the ANSTO Antares AMS Facility (Fink and Smith, 2007) and were normalised to the 2007 KNSTD standard KN01-5-2 with a nominal  $^{10}\text{Be}/^{9}\text{Be}$

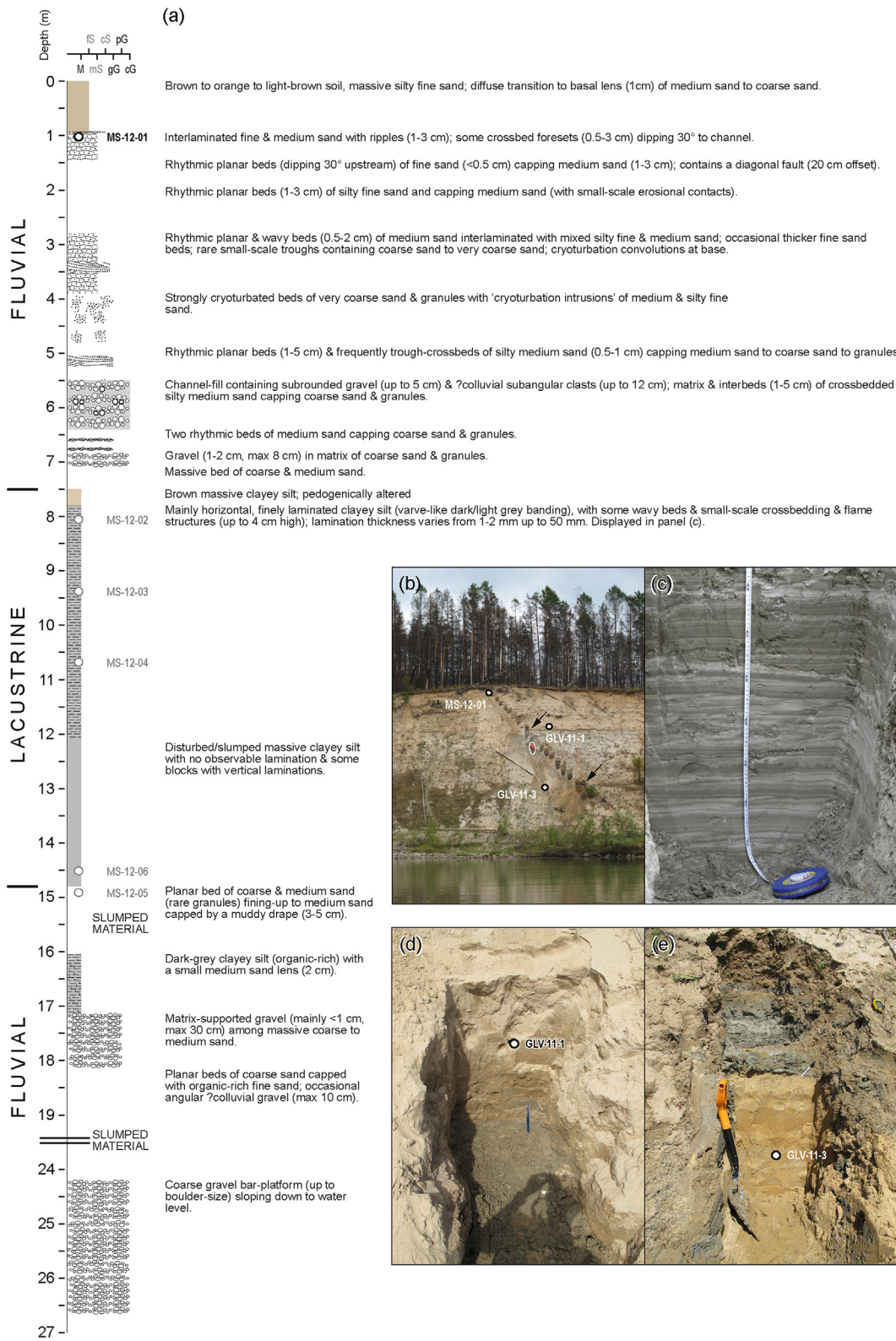


**Fig. 5. Myya-left bank main lacustrine section** [56.421°N, 115.536°E]; location shown in Fig. 2. (a) Stratigraphic stack of the 27 m-high river bank section as logged in 2012. The section is topped by a flattish and forested terrace (~505 m a.s.l.), which ramps up to ~4–5 m higher along the upstream part of the exposure. Abbreviations in the grain-size key: M – silt, fS – fine sand, mS – medium sand, cS – coarse sand, gG – granule, pG – pebble, and cG – cobble. Locations of OSL samples collected in 2012 are indicated (samples that did not yield ages are in grey). (b) View of the section in 2012 – see person for scale (white ellipse). The unit of glaciolacustrine muds is marked by arrows. Locations of all OSL samples yielding an age is indicated. (c) Laminations of silt and minor fine-sand (light-grey) and clays (dark-grey) in the glaciolacustrine unit, with occasional cross-bedding and no identifiable traces of organic matter. (d) View of the position of OSL sample GLV-11-1 collected in 2011 from fluvial sands above the glaciolacustrine muds – note the sharp contact between the units at the bottom of the pit. (e) View of the position of OSL sample GLV-11-3 collected in 2011 from fluvial sands below the glaciolacustrine muds – note the sharp contact between the units. See Fig. 12 for the derived ages.

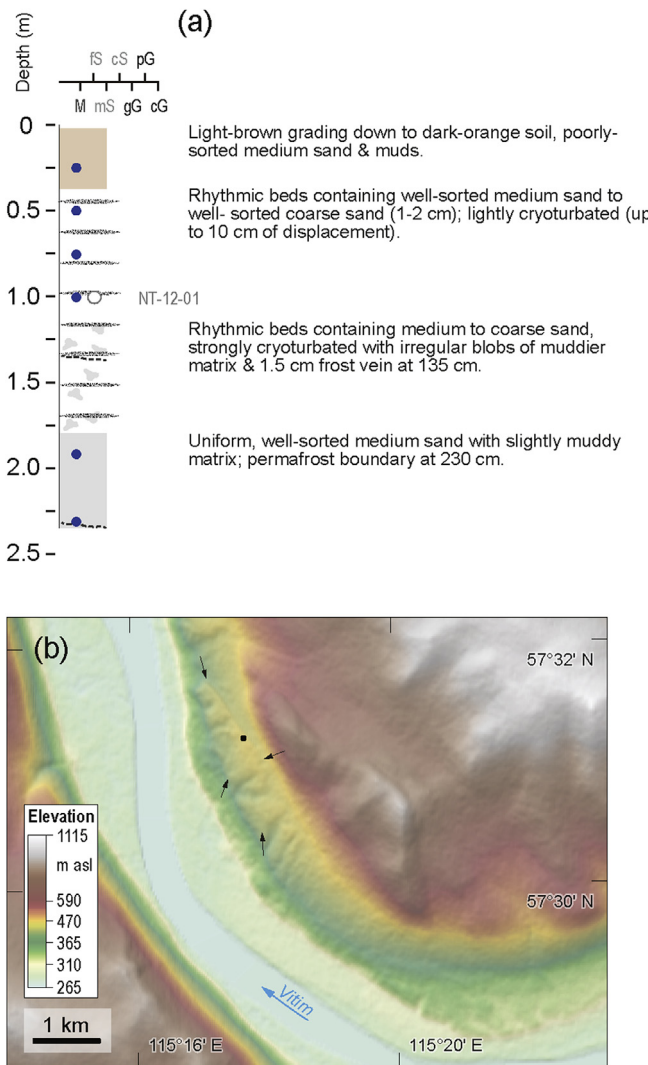


**Fig. 6.** Giant eddy bar at Nerpo [57.521 °N, 115.296 °E]; location shown in Fig. 2. (a) Stratigraphic stack logged in a pit excavated on the crest of the bar (location marked by a black dot in panel b). Samples constituting the  $^{10}\text{Be}$  depth profile are drawn in blue (see Fig. 12 for the derived age), location of the OSL sample is also indicated. Grain-size attributes are drawn as in Fig. 5. (b) Hillshade image derived from SRTM 1-arc-sec elevation data draped with colour hypsometry. Outline of the bar is marked by arrows. (For interpretation of the references to colour in this figure legend, the reader is referred to the Web version of this article.)

ratio of  $8.56 \times 10^{-12}$  (Nishiizumi et al., 2007). Errors for the final  $^{10}\text{Be}$  concentrations (atoms/g) for all samples (GLV, BUP, and NT) were calculated by summing in quadrature the statistical error for the AMS measurement, 2% for reproducibility, and 1% for uncertainty in the Be spike concentration.

**3.2.2.1. Monte Carlo-based modelling of depth profiles and exposure calculations.**  $^{10}\text{Be}$  deposition ages for the depth profiles were calculated using the age calculator code of Hidy et al. (2010; version 1.2) available from <http://geochronology.earthsciences.dal.ca>. The modelled Bayesian 'most probable age' and associated uncertainties are obtained from relative probability density functions constructed from all the ages generated from a customised Monte Carlo simulation. The calculator uses a time-independent spallation production model based on the St scaling scheme (Stone, 2000). Muon production is calculated using Heisinger et al. (2002a, b) following the approach of Balco et al. (2008) and thus results are

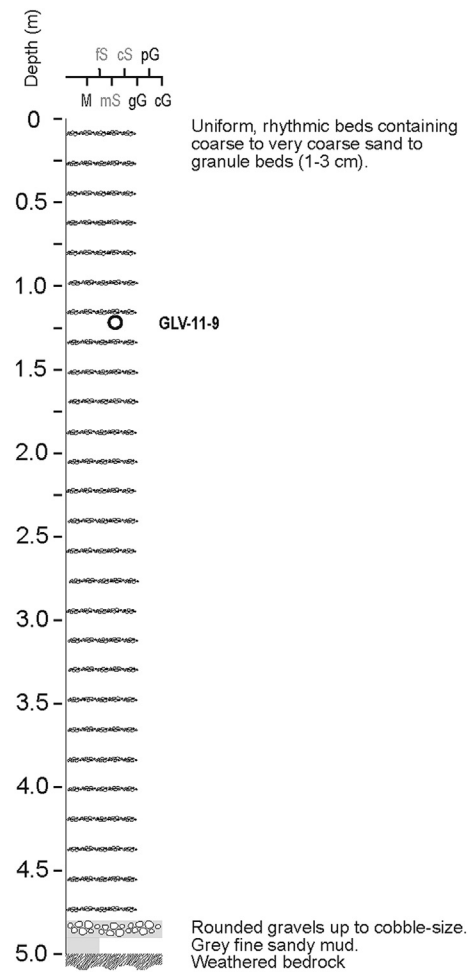


**Fig. 7.** Giant eddy bar at Bur [57.882 °N, 114.351 °E]; location shown in Fig. 2. Stratigraphic stack logged in a sand extraction pit in the giant bar at Bur. Position of OSL sample GLV-11-9 is indicated (see Fig. 12 for the derived age). Grain-size attributes are drawn as in Fig. 5.

compatible with the online calculators formerly known as the CRONUS online calculators. We use a modified global average  $^{10}\text{Be}$  sea-level and high-latitude spallation production rate of  $3.99 \pm 0.22$  atoms  $\text{g}^{-1} \text{yr}^{-1}$  (Heyman, 2014), which is derived from the St scaling scheme, and is statistically identical to the recent  $^{10}\text{Be}$  spallation production rates reported in Borchers et al. (2016). Bedrock exposure ages for the 8 GLV samples were calculated using the online calculators formerly known as the CRONUS online calculators (Balco et al., 2008; version 2.2; constants 2.2.1) and, for consistency with our depth profile ages, are reported here using the St production rate scaling, with the same reference spallation production rate of  $3.99 \pm 0.22$  atoms  $\text{g}^{-1} \text{yr}^{-1}$ . We adopt the  $^{10}\text{Be}$  half-life of  $1.387 \pm 0.012$  Ma (Chmeleff et al., 2010; Korschinek et al., 2010) in all our calculations.

### 3.3. Quantifying peak discharge of the outburst floods

Neither the details of the ice-dam breach mechanism, nor the size of the breach and its rate of growth are known. Thus, we opted for a conservative estimate of peak discharge based on unequivocal minimum floodstages indicated by a series of high eddy/expansion bars developed along the Vitim valley (Fig. 2, Table 4). We applied the one-dimensional step-backwater hydraulic model, HEC-RAS (Hydrologic Engineering Center, 2010, version 4.1), in order to



**Fig. 8. Giant eddy-bar exposures at Bodaybo.** Proximal portion of an eddy-bar partially blocking the Bodaybo River tributary to the Vitim River (see Fig. 2), with (a), possibly ice rafted block ( $1 \times 2 \times 2.5$  m) and boulder cluster [57.844 °N, 114.152 °E]. (b) High-energy, suspension-load deposit (~7 m thick) of planar coarse sands (1–3 cm thick) interbedded with matrix-supported gravels (up to 8 cm diameter) [57.846 °N, 114.149 °E]. (c) Eddy-bar deposits at 'Upper Pit' [57.922 °N, 114.219 °E]: ~13 m of rhythmic, planar interlaminated coarse and fine sands, coarsening-downwards to ~30 cm beds of coarse sands and angular, matrix-supported gravels (up to 60 cm diameter); all overlain by a ~1 m aeolian sand sheet (white dash boundary). Shown are OSL samples (black circles) and samples (blue dots) constituting the  $^{10}\text{Be}$  depth profile (see Fig. 12 for the derived ages). Stratigraphic stack (right-panel) indicates grain-size attributes for the section seen in panel c (see Fig. 5 caption for abbreviations in the grain-size key): (d) Close-up of a 5 m thick unit of mostly open-work gravels (5–15 cm diameter) indicating rapid deposition from high-energy flow [57.851 °N, 114.159 °E]. (For interpretation of the references to colour in this figure legend, the reader is referred to the Web version of this article.)

**Table 1**  
**Summary table of OSL data** with burial depth and elevation as used for calculation of cosmic dose rate, assumed average sediment moisture during burial (mod. = modelled, see text), the concentration of dose rate relevant elements (K, Th, U), total dose rate (D), number of accepted aliquots (n), the overdispersion value (od.), mean Equivalent dose ( $D_e$ ) and the resulting OSL age. For six of the samples no OSL age was calculated because of [1] all aliquots being contaminated by feldspar signals, [2] only three aliquots passing rejection criteria, [3] complex distribution of Equivalent dose (Fig. 13) with ambiguous application of the Minimum Age Model, or [4] low OSL signal level and potential contamination by medium component.

Sample	Depth (cm)	Elevation (m)	W (%)	K (%)	Th (ppm)	U (ppm)	D (Gy $\text{ka}^{-1}$ )	n	od.	$D_e$ (Gy)	Age (ka)
<b>Mya River sedimentary section (56.421 °N/115.536 °E)</b>											
GLV-11-1	700	495	mod.	$2.89 \pm 0.09$	$6.80 \pm 0.30$	$1.62 \pm 0.20$	$3.26 \pm 0.21$	31	0.10	$71.1 \pm 1.6$	$21.8 \pm 1.5$
GLV-11-3	1800	484	mod.	$2.94 \pm 0.15$	$5.82 \pm 0.24$	$1.24 \pm 0.18$	$3.04 \pm 0.28$	28	0.25	$105.3 \pm 5.7$	$34.6 \pm 3.7$
MS-12-01	100	501	$8 \pm 4$	$2.68 \pm 0.15$	$5.42 \pm 0.24$	$1.25 \pm 0.20$	$3.17 \pm 0.26$	15	0.42	$36.79 \pm 4.07$	$11.6 \pm 1.6$
MS-12-01	100	501	$8 \pm 4$	$2.68 \pm 0.15$	$5.42 \pm 0.24$	$1.25 \pm 0.20$	$3.17 \pm 0.26$	15	MAM	$29.82 \pm 5.89$	$9.4 \pm 2.0$
MS-12-02	810	494	$15 \pm 5$	$3.24 \pm 0.16$	$11.10 \pm 0.50$	$2.51 \pm 0.21$	—	—	—	—	[1]
MS-12-03	940	493	$15 \pm 5$	$3.07 \pm 0.16$	$8.50 \pm 0.40$	$2.22 \pm 0.18$	—	3	0.16	$47.7 \pm 4.8$	[2]
MS-12-04	1070	491	$25 \pm 5$	$3.01 \pm 0.10$	$7.00 \pm 0.30$	$1.76 \pm 0.22$	—	34	0.59	$49.1 \pm 5.2$	[3]
MS-12-05	1490	487	$15 \pm 5$	$2.74 \pm 0.14$	$5.90 \pm 0.30$	$1.64 \pm 0.23$	—	—	—	—	[1]
MS-12-06	1450	487	$15 \pm 5$	$3.03 \pm 0.15$	$7.10 \pm 0.30$	$1.86 \pm 0.15$	—	3	0.21	$30.9 \pm 3.9$	[2]
<b>Nerpo (57.521 °N/115.296 °E)</b>											
NT-12-01	470	470	$20 \pm 10$	$2.52 \pm 0.13$	$6.30 \pm 0.30$	$1.76 \pm 0.18$	—	12	—	—	[4]
<b>Bur (57.881 °N/114.351 °E)</b>											
GLV-11-9	120	367	$20 \pm 10$	$2.60 \pm 0.13$	$6.60 \pm 0.30$	$1.33 \pm 0.16$	$2.87 \pm 0.34$	18	0.24	$42.8 \pm 2.8$	$14.9 \pm 2.0$
<b>Bodaybo 'Upper Pit' (57.922 °N/114.219 °E)</b>											
GLV-11-5	100	341	$20 \pm 10$	$2.37 \pm 0.12$	$6.90 \pm 0.30$	$1.71 \pm 0.19$	$2.80 \pm 0.32$	21	0.20	$93.3 \pm 4.7$	$33.3 \pm 4.2$
GLV-11-7	1400	328	$20 \pm 10$	$2.50 \pm 0.08$	$10.40 \pm 0.40$	$2.14 \pm 0.21$	$3.05 \pm 0.34$	24	0.12	$103.9 \pm 4.0$	$34.1 \pm 4.0$
BUP-12-01	25	342	$20 \pm 10$	$2.34 \pm 0.12$	$7.60 \pm 0.30$	$1.86 \pm 0.18$	$2.81 \pm 0.32$	16	0.19	$55.1 \pm 3.1$	$19.6 \pm 2.5$

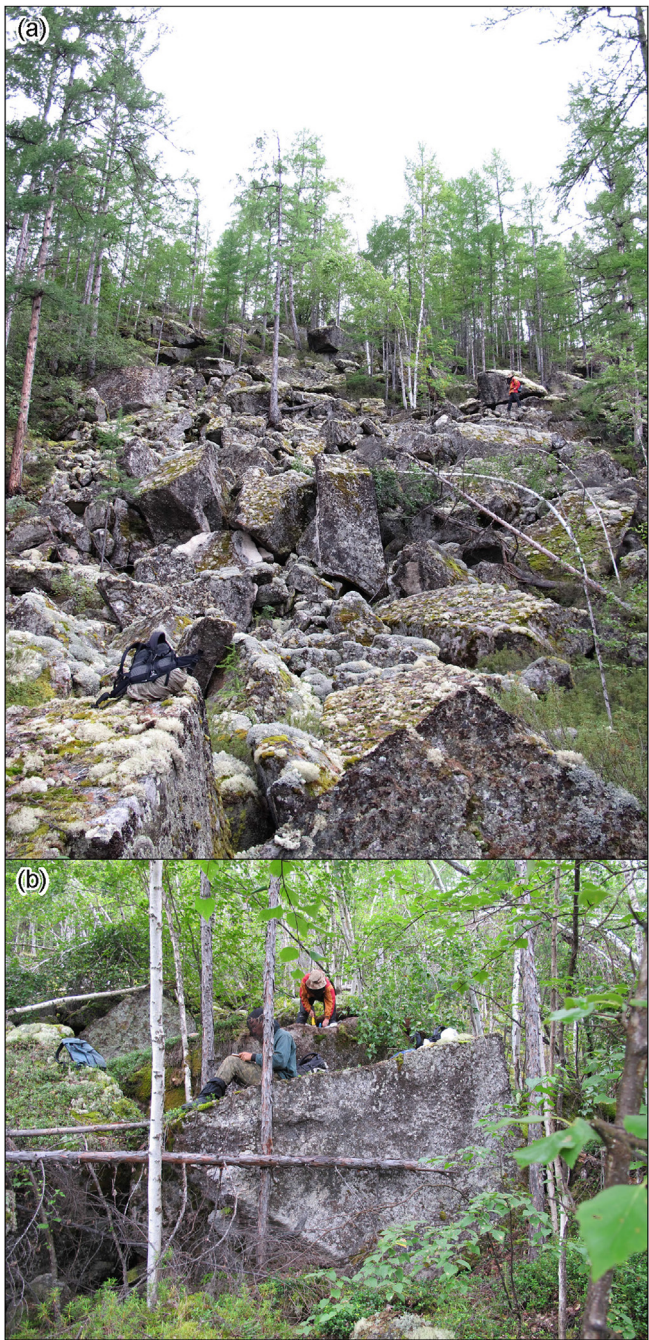


**Fig. 9. Spillway talus slope.** (a) View looking up to the spillway rim from near the base of the talus slope, note person for scale. (b) Sampling a large talus block (GLV-9;  $7 \times 7 \times 2$  m,  $57.3917^\circ$ N,  $116.4917^\circ$ E) midway down the talus slope for  $^{10}\text{Be}$  exposure dating ( $24.7 \pm 1.7$  ka). The block is pinned between other large blocks ( $\sim 3 \times 2$  m &  $\sim 1 \times 1$  m). See Fig. 3 for location.

obtain a minimum estimate of the peak discharge of floods responsible for the highest eddy/expansion bars. The widely applied HEC-RAS model produces an energy-balanced water-surface profile as a function of discharge, roughness, and flow geometry. This simple one-dimensional model is most appropriate for our reconstruction of the Vitim megafloods, because floodstage is the only available source of palaeoflow data and in principle the quality of data input should dictate the level of modelling complexity (Carling et al., 2003). Accordingly, the modelling outputs provide approximations only. In addition, we applied three

simple empirical equations for estimating peak discharge based on dimensions of the impoundment and the breach – these are introduced together with the discharge values in Section 4.3.2.

### 3.3.1. HEC-RAS methods

The flood modelling was applied to the ~520 km reach of the Vitim River from the area of the ice dam (near Lake Oron) to the Lena River junction (Fig. 2). Flow geometry was reconstructed following standard procedures using Shuttle Radar Topographic Mission 1-arc-sec digital elevation data coupled to the HEC-GeoRAS (Hydrologic Engineering Center, 2011) extension in ArcGIS 10.2 (Environmental Systems Research Institute, 2011).

We manually defined 253 valley cross-sections (spaced roughly every 2 km) and then exported the data to HEC-RAS. We assumed a fixed channel boundary for the flow modelling based on present-day channel morphology. Although we anticipate that the megafloods locally scoured the former valley fill to bedrock, scour depth is a small fraction of the full flow cross-section and therefore any resulting discharge underestimation is minor relative to other sources of error.

We ignored tributary inputs along the modelled reach, as any contributing discharge would be comparatively negligible. The tributaries and their junctions act primarily as discharge storage zones during megafloods: Vitim floodwaters moved up tributaries and then re-entered the Vitim mainstem during waning stages. In this way, flood deposits were emplaced at junctions and up some tributary valleys; e.g., Bodaybo River 'Upper Pit' ~15 km upstream of the Vitim junction (Fig. 2). Tributary mouths and other areas of flow expansion likely to develop flow separation eddies were defined as 'ineffective flow' zones (in 78 of the 253 cross-sections); tributaries close to the former ice-dam (e.g., Amalyk River; Fig. 3) were very likely blocked with ice and so were defined as 'blocked obstructions' (in 9 cross-sections).

The ~520 km longitudinal profile of the modelled Vitim River reach is smoothly concave (Fig. 10a). Average bed slope at the upstream end is ~0.50 m/km, declining to ~0.15 m/km just above the Lena River junction. Outbursts from glacial Lake Vitim resulted in deep flows that were confined within the narrow Vitim valley in a setting comparable to megafloods from Lake Chuja-Kuray (Herget, 2005). Yet, the Vitim River is considerably less steep than the Chuja-Katun River (Chuja River ~6 m/km, Katun River ~2.2 m/km; [Herget, 2005]); hence, flow velocities and energy losses in general are expected to be somewhat lower. Energy losses in HEC-RAS are accommodated via coefficients for flow expansion and contraction and by the roughness coefficient, Manning's *n*. The history of glacial erosion along the Vitim (Margold and Jansson, 2011) has left a remarkably uniform valley width downstream; hence we retained the HEC-RAS default values for expansion and contraction at 0.1 and 0.3, respectively. To account for uncertainties with predicting the roughness of flows >200 m deep we used a range of Manning's *n* from 0.03 to 0.05, following other megaflood reconstructions (Herget, 2005; Carling et al., 2010).

Consistent with previous megaflood modelling (O'Connor and Beebe, 2009; Bohorquez et al., 2016), we anticipated generally subcritical flow conditions possibly with local transcritical flow zones. Accordingly, the HEC-RAS model runs were conducted under conditions of 'mixed regime' steady uniform flow initiated by 'normal depth' floodstage at the downstream and upstream cross-sections (using bed slopes given above). We consider the giant flood bars were constructed rapidly during the steady flow conditions that followed the initial flood wave after the ice-dam breach.

## 4. Results and interpretations

The new evidence we present for the existence of glacial Lake

**Table 2**Summary of bedrock sample  $^{10}\text{Be}$  results and exposure ages.

Sample Code	Latitude/Longitude ( $^{\circ}\text{N} / ^{\circ}\text{E}$ )	Elevation (m a.s.l.)	Sample thickness <sup>a</sup> (cm)	Topographic shielding factor	Quartz <sup>b</sup> Mass (g)	Be spike ( $\mu\text{g}$ )	$^{10}\text{Be}/^{9}\text{Be}^{\text{c}}$ ( $\times 10^{-15}$ )	$^{10}\text{Be}$ Concentration <sup>c</sup> ( $\times 10^3$ atoms $\text{g}^{-1}$ $\text{SiO}_2$ )	Exposure age <sup>c,d</sup> (ka)
<b>Flood I spillway</b>									
GLV-1	57.39436/116.49013	478	2	0.99922	37.49	273.7	$772.4 \pm 25.3$	$376.86 \pm 12.82$	$59.1 \pm 3.9$
GLV-3	57.40051/116.49645	578	2.5	0.99927	37.54	268.1	$792.1 \pm 26.4$	$377.98 \pm 13.08$	$54.1 \pm 3.6$
GLV-5	57.39310/116.49051	487	2	0.99917	37.30	272.1	$738.3 \pm 24.4$	$359.86 \pm 12.35$	$55.9 \pm 3.7$
GLV-7	57.39114/116.49090	480	3	0.99904	37.67	273.6	$721.1 \pm 24.0$	$349.98 \pm 12.11$	$55.2 \pm 3.6$
<b>Spillway talus block</b>									
GLV-9	57.39172/116.49166	452	2	0.97792	37.29	273.7	$309.1 \pm 11.4$	$151.60 \pm 5.79$	$24.7 \pm 1.7$
<b>Oron delta talus block</b>									
GLV-15	57.2218/116.40675	363	3	0.98063	36.22	274.3	$158.3 \pm 6.4$	$80.11 \pm 3.32$	$14.3 \pm 1.0$
<b>Oron delta moraine</b>									
GLV-11	57.15510/116.33270	436	2	0.998	37.62	274.0	$248.0 \pm 9.9$	$120.62 \pm 4.93$	$19.5 \pm 1.3$
GLV-13	57.15567/116.33258	427	3	0.998	36.03	273.4	$238.0 \pm 9.3$	$120.79 \pm 4.83$	$19.9 \pm 1.4$

<sup>a</sup> The tops of all samples were exposed at the surface.<sup>b</sup> A density of  $2.7 \text{ g cm}^{-3}$  was used based on the granitic composition of the samples.<sup>c</sup> All uncertainties are reported at the 1-sigma level. Blank corrected 10/9 ratios. See text for details on level of blanks.<sup>d</sup> Exposure ages were calculated with the online calculator formerly known as CRONUS (Balco et al., 2008), version 2.2; constants 2.2.1; (<http://hess.ess.washington.edu/>), using  $^{10}\text{Be}$  SLHL production rate of Heyman (2014). See text for full details of the cosmogenic  $^{10}\text{Be}$  analyses and exposure age calculations.**Table 3**Summary of  $^{10}\text{Be}$  results in depth profile samples.

Sample Code	Depth below surface (cm)	Sample thickness (cm)	Quartz Mass (g)	Be spike ( $\mu\text{g}$ )	$^{10}\text{Be}/^{9}\text{Be}^{\text{a}}$ ( $\times 10^{-15}$ )	$^{10}\text{Be}$ Concentration <sup>a</sup> ( $\times 10^3$ atoms $\text{g}^{-1}$ $\text{SiO}_2$ )
<b>Nerpo (57.521 °N/115.296 °E; 471 m a.s.l.)</b>						
NT-345	25	4	15.78	327.3	$133.3 \pm 4.5$	$184.80 \pm 7.49$
NT-470	50	4	17.31	327.6	$121.5 \pm 4.1$	$153.76 \pm 6.24$
NT-595	75	4	28.09	331.8	$149.4 \pm 3.5$	$117.90 \pm 3.80$
NT-6-120	100	4	20.70	327.3	$108.7 \pm 3.4$	$114.90 \pm 4.37$
NT-8-212	192	4	17.32	326.8	$85.6 \pm 2.9$	$107.95 \pm 4.38$
NT-1-255	235	4	7.93	328.5	$35.8 \pm 2.2$	$99.00 \pm 6.42$
<b>Bodaybo 'Upper Pit' upper section (57.922 °N/114.219 °E; 351 m a.s.l.)</b>						
BUP-01	7.5	5	61.57	332.0	$533.1 \pm 8.9$	$192.30 \pm 5.37$
BUP-03	25	4	17.18	326.5	$155.1 \pm 6.9$	$196.98 \pm 9.82$
BUP-04	45	4	19.30	325.5	$152.1 \pm 4.9$	$171.45 \pm 6.74$
BUP-05	65	4	22.12	324.9	$166.0 \pm 4.5$	$162.91 \pm 5.75$
BUP-06	85	4	30.17	331.0	$203.1 \pm 5.0$	$148.90 \pm 4.95$
<b>Bodaybo 'Upper Pit' lower section (57.922 °N/114.219 °E; 351 m a.s.l.)</b>						
BUP-07	105	4	24.23	327.8	$218.8 \pm 7.0$	$198.00 \pm 7.74$
BUP-08	145	4	32.85	326.4	$196.0 \pm 5.0$	$130.16 \pm 4.41$
BUP-09	185	4	21.71	326.7	$106.2 \pm 3.7$	$106.75 \pm 4.39$
BUP-11	265	4	38.78	327.5	$132.2 \pm 3.3$	$74.62 \pm 2.52$
BUP-13	445	4	26.39	327.2	$76.0 \pm 3.3$	$62.97 \pm 3.05$
BUP-15	845	4	29.10	327.1	$85.0 \pm 3.5$	$63.89 \pm 3.00$
<b>Bodaybo 'Upper Pit' lower section corrected for deposition age of Bodaybo upper section</b>						
BUP-07	105	4				$173.33 \pm 10.45$
BUP-08	145	4				$114.57 \pm 6.25$
BUP-09	185	4				$96.71 \pm 5.24$
BUP-11	265	4				$70.09 \pm 2.83$
BUP-13	445	4				$61.56 \pm 3.08$
BUP-15	845	4				$63.24 \pm 3.01$

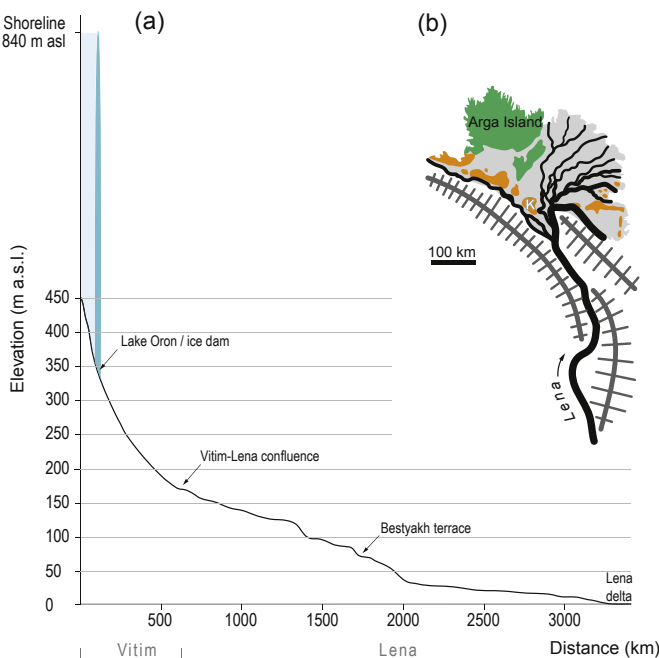
<sup>a</sup> All uncertainties are reported at the 1-sigma level. Blank corrected 10/9 ratios. See text for details on level of blanks.

Vitim and its outburst floods consists principally of the thick unit of glaciolacustrine muds exposed in the bank of the Muya River (Fig. 5) and of the giant eddy bars strewn along the Vitim valley downstream from the ice-dam area (Figs. 2, 6–8). These are massive, coarse-gravel and sand deposits perched up to ~230 m above the Vitim River and their position at inner bends and tributary junctions suggests they developed via flow-separation during very deep flows. Sedimentary exposures at Bodaybo (Fig. 8) reveal ~30 m-thick, rhythmically-bedded sand, and up to 5 m of open-work coarse gravels deposited rapidly from

suspension—structures diagnostic of extreme floods (Carling, 2013). Besides those giant bars investigated in the field, we mapped a number of others from the SRTM 1 arc-sec data (Figs. 2 and 11). In the following, we first summarise the dating results (Section 4.1) and proceed to reconstruct the chronology of the outburst floods (Section 4.2.) as well as their peak discharge (Section 4.3.). We then return upstream to the Muya-Kuanda Depression to reconstruct its sedimentary environment (Section 4.4.), which is important not only for gaining better knowledge of the Quaternary history of the region but also in order to allow for a comparison

**Table 4**Giant-bar floodstage indicators along the Vitim valley (upstream to downstream).<sup>a</sup>

Bar type & position	Latitude (dd)	Longitude (dd)	Bar-crest elevation (m asl)	Elevation above river level (m)	Distance downstream of Lake Oron (ice-dam area) (km)
Expansion bar, upstream of constriction <sup>b</sup>	57.7024	116.2698	436	129	70
Eddy bar at Nerpo, inside-bend	57.5210	115.2958	471	204	153
Eddy bar complex at Bur (crest), inside-bend	57.8832	114.4073	466	233	232
Eddy-bar complex at Bodaybo R tributary-mouth	57.8473	114.1629	328	99	259
Eddy bar at Mamakan, inside-bend	57.8140	113.9811	307	80	270
Eddy bar, inside-bend <sup>b</sup>	57.9091	113.5863	371	152	302
Expansion bar, downstream of constriction <sup>b,c</sup>	58.9409	112.8342	302	120	451
Eddy bar, tributary-mouth <sup>b</sup>	59.2696	112.8281	303	129	505

<sup>a</sup> Geographical coordinates & elevations taken from Google Earth in decimal degrees and metres above sea level, respectively.<sup>b</sup> Sites not visited in the field —interpreted from DEM and remote imagery.<sup>c</sup> The largest known flood bar on the Vitim: ~5 × 2 km (see Fig. 11).

**Fig. 10. (a) Vitim-Lena river long profile.** Valley profile extending from the Muya-Kuanda Depression to the Lena Delta (derived from SRTM 1-arc-sec data). **(b) Lena Delta schematic map.** At the Arctic coast and just before meeting its delta, the Lena River passes between the steep Chekanovsky and Kharaulakh ridges. The bedrock constriction focuses erosive power at the delta apex and drastically lowers the preservation potential of sediments on the proximal Kurungnakh-Sise Island (K; Wetterich et al., 2008). The two major erosional terrace remnants on the delta are shown: the Arga Complex, 20–30 m a.s.l. (green) and Ice Complex, 30–55 m a.s.l. (orange), in addition to the modern active accumulation zone, 1–12 m a.s.l. (grey; Schwamborn et al., 2002; Schirrmeister et al., 2011). This map is redrawn from Wetterich et al. (2008). (For interpretation of the references to colour in this figure legend, the reader is referred to the Web version of this article.)

with the geological and geomorphological record of high-magnitude glacial lake outburst floods elsewhere.

#### 4.1. Summary of the geochronology

##### 4.1.1. OSL ages

The OSL ages are summarised in Table 1 and Fig. 12. For most samples, we found a prominent contamination of the quartz signal by feldspar that could not be removed by additional etching and sieving. Four samples were abandoned as an insufficient number of aliquots delivered pure quartz OSL signals (Fig. 13a). In sample NT-12-01 most aliquots exhibit no OSL signal or a signal dominated by an unstable medium component (see Steffen et al., 2009). In five of

the remaining samples, Equivalent Dose values are mainly tightly and normally distributed (Fig. 13b), indicating the presence of a large population of aliquots in which the OSL signal was likely zero at the time of deposition. We applied the Central Age Model (CAM) for all samples except one in which we applied the Minimum Age Model (Galbraith et al., 1999) to identify the well-bleached population and the resulting value for age calculation.

##### 4.1.2. Cosmogenic $^{10}\text{Be}$ ages

CRONUS-derived bedrock exposure ages are summarised in Table 2 and depth profile  $^{10}\text{Be}$  data in Table 3; all are displayed in Fig. 12. Monte Carlo model parameters are summarised in Table 5 and model results in Fig. 14. The Bayesian most probable age obtained for the Nerpo depth profile is 17.7 ka (with  $\pm 1\sigma$  limits of 22.3–14.6 ka). These uncertainty bounds are calculated directly from the probability density function constructed from the age results (Fig. 14c). The sedimentary section in Bodaybo 'Upper Pit' consists of >10 m of flood-deposited sands and gravels capped by a unit of aeolian origin ~1 m thick (Fig. 8c). Thus, the measured  $^{10}\text{Be}$  inventory of the lower portion of Bodaybo 'Upper Pit' section is composed of (i)  $^{10}\text{Be}$  accumulated prior to the emplacement of the upper aeolian unit, and (ii)  $^{10}\text{Be}$  accumulated after aeolian deposition at a substantially lower production rate. Accordingly, to calculate an age for the lower portion of the Bodaybo 'Upper Pit' section, the  $^{10}\text{Be}$  accumulated after the emplacement of the aeolian unit needs to be calculated and subtracted from the measured  $^{10}\text{Be}$  values. In the case of the Bodaybo samples, this  $^{10}\text{Be}$  component represents between 12 and 1% of the total measured  $^{10}\text{Be}$  concentration in the top and bottom lower portion samples, respectively.

The Bayesian most probable age obtained for the aeolian unit of Bodaybo 'Upper Pit' section is 15.2 ka (with  $\pm 1\sigma$  limits of 19.6–11.3 ka). We obtain a Bayesian most probable age for the lower portion of the Bodaybo 'Upper Pit' section (immediately before the emplacement of the upper aeolian unit) of 19.7 ka (with  $\pm 1\sigma$  limits of 24.1–16.8 ka). Summing the two ages we obtain a final age for the flood deposit in the lower portion of the Bodaybo 'Upper Pit' section of 34.9 ka (with  $\pm 1\sigma$  limits of 41.1–30.0 ka).

The four  $^{10}\text{Be}$  samples (GLV-1,3,5,7, Figs. 3 and 12, Table 2) taken from the rim of the spillway yield a weighted-mean of  $56.0 \pm 1.8$  ka (standard mean error; Fig. 12, Table 2), but given the possibility of some surface weathering this should be regarded as a minimum. Although relevant rock weathering data could not be located for Siberia, in order to quantify the potential effect of surface erosion on the spillway exposure ages, we model a range of erosion rates based on published weathering data from similar granitic rock surfaces in Arctic northern Sweden (André, 2002). Reported surface weathering rates range between 0.2 and 1.0 mm  $\text{ka}^{-1}$ , and when applied to our samples, these yield weighted-mean surface exposure ages between  $56.5 \pm 1.9$  and  $61.8 \pm 2.3$  ka, respectively.

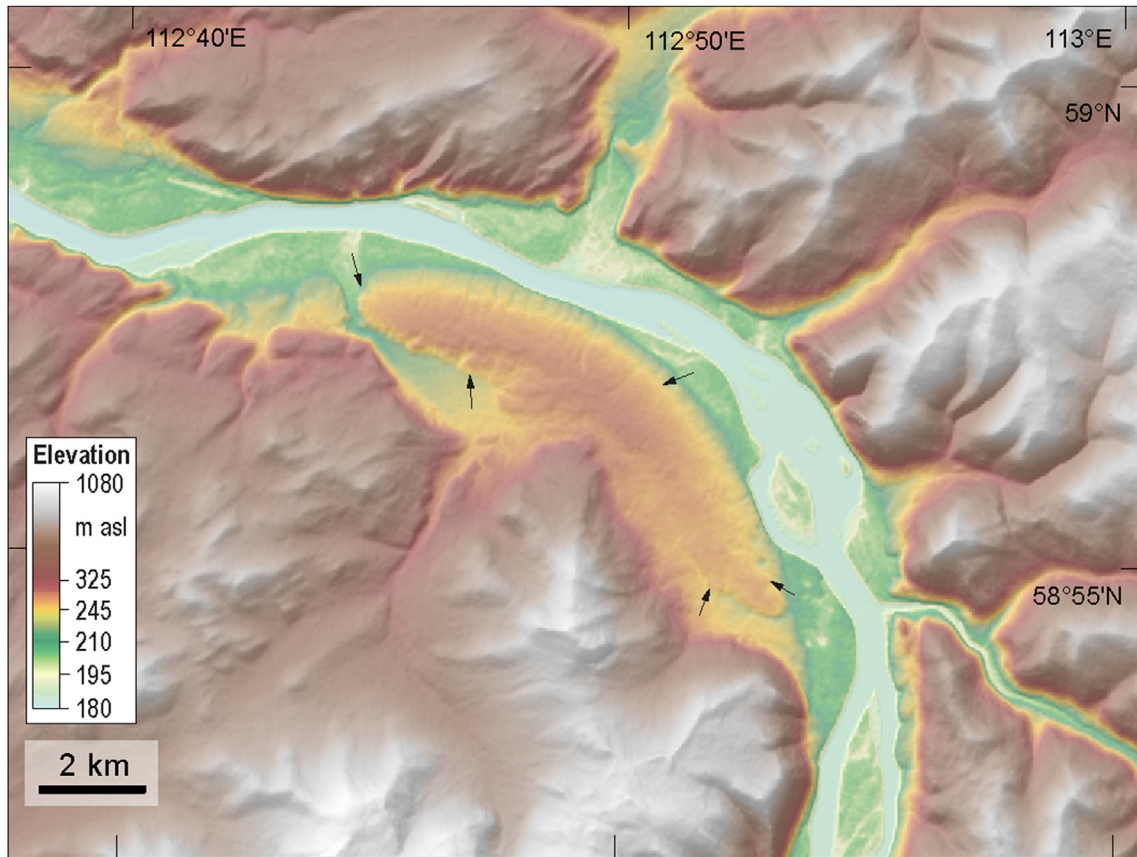


**Fig. 11.** Plan view of the best-developed giant eddy bar on the Vitim [58.9409°N, 112.8342°E] in a hillshade image derived from SRTM 1-arc-sec elevation data draped with colour hypsometry. The giant bar is developed on the inside convex-bend of the lower Vitim (see Fig. 2 for location) and is the largest known eddy bar on the Vitim River: ~5 km long, ~2 km wide and with a crest standing ~120 m above river level. Outline of the bar is marked by arrows. (For interpretation of the references to colour in this figure legend, the reader is referred to the Web version of this article.)

#### 4.2. Reconstructed flood chronology

Our reconstruction identifies at least three outburst floods from glacial Lake Vitim over the past ~60 ka (Fig. 15). The oldest, Flood-I, formed the 300 m deep spillway when meltwater overtopped and incised the ice-dam to its base, eroding ~3 km<sup>3</sup> of underlying bedrock, although we cannot rule out the cumulative effect of earlier overspills (Bjornstad et al., 2001; Larsen and Lamb, 2016). Carving of the spillway reflected the configuration of the ice dam and we surmise that an ice-cap downstream of Lake Oron probably blocked the Vitim valley and buried the surrounding lower mountains in ice (Figs. 2 and 16). The four <sup>10</sup>Be samples from the rim of the spillway yield a minimum (zero-erosion) weighted mean exposure age of 56.0 ± 1.8 ka and provide an estimated timing of Flood I (Fig. 15).

Flood-II is dated via OSL and Bayesian Monte Carlo analysis (Hidy et al., 2010) of a <sup>10</sup>Be depth-profile on a giant bar ~130 m above Vitim River at the Bodaybo 'Upper Pit' site (Fig. 12). Two statistically equivalent OSL dates: 33.3 ± 4.2 ka and 34.1 ± 4.0 ka (GLV-11-5 and -7; Fig. 12, Table 1) demonstrate rapid deposition of a 13 m stack of rhythmically-bedded sands and gravels. The <sup>10</sup>Be depth-profile yields a Bayesian most probable age of 34.9 ka (with ±1 σ limits of 41.1–30.0 ka; Tables 3 and 5, Figs. 12 and 14). We traced the Flood-II source ~400 km upstream to the Muya-Kuanda Depression (as for all floods) where Lake Vitim deposited 11 m of laminated glaciolacustrine muds now exposed in the banks of the Muya River (Figs. 2 and 5). Fluvial sands predating the lake yield an

OSL age of 34.6 ± 3.7 ka (GLV-11-3), whereas fluvial sands capping the muds yield 21.8 ± 1.5 ka (GLV-11-1; Fig. 12, Table 1). These two ages provide maximum and minimum-limiting bounds.

Three sites constrain the timing of Flood-III: an OSL age of 14.9 ± 2.0 ka from the giant eddy bar at Bur (GLV-11-9; Fig. 12, Table 1), a Bayesian most probable <sup>10</sup>Be depth-profile age of 17.7 <sup>+4.6</sup>/<sub>-3.1</sub> ka on the giant eddy bar at Nerpo (Tables 3 and 5, Fig. 12), and two <sup>10</sup>Be exposure ages of 19.5 ± 1.3 and 19.9 ± 1.4 ka from boulders topping the Oron moraine (Margold et al., 2016, Table 2 and Fig. 12), which postdate the megafloods.

Overall, our outburst chronology accords with the regional glacial history (Margold et al., 2016): Flood-I occurred during deglaciation following OIS-4; Flood-II, in the build-up to the local Last Glacial Maximum; and Flood-III, during the last deglaciation (Fig. 15 and Table 6). The notion that Flood I carved the giant spillway is consistent with the fact that earlier glaciations are thought to have been more extensive than the local Last Glacial Maximum (Zolotarev, 1974; Bazarov et al., 1981; Bazarov, 1986; Enikeev, 2008, 2009; Margold et al., 2016). Whereas Flood-I cut through an extensive ice dam (Figs. 12 and 16a) and incised the spectacular bedrock spillway, Floods II and III were largely limited to the Vitim valley and may have been responsible for the trimming of the valley slopes immediately downstream of Lake Oron (Figs. 3, 12, 16b).

We propose a coherent chronological model of glacial Lake Vitim megaflooding, while acknowledging that not all ages in our dataset conform perfectly. In particular, two <sup>10</sup>Be ages cannot be

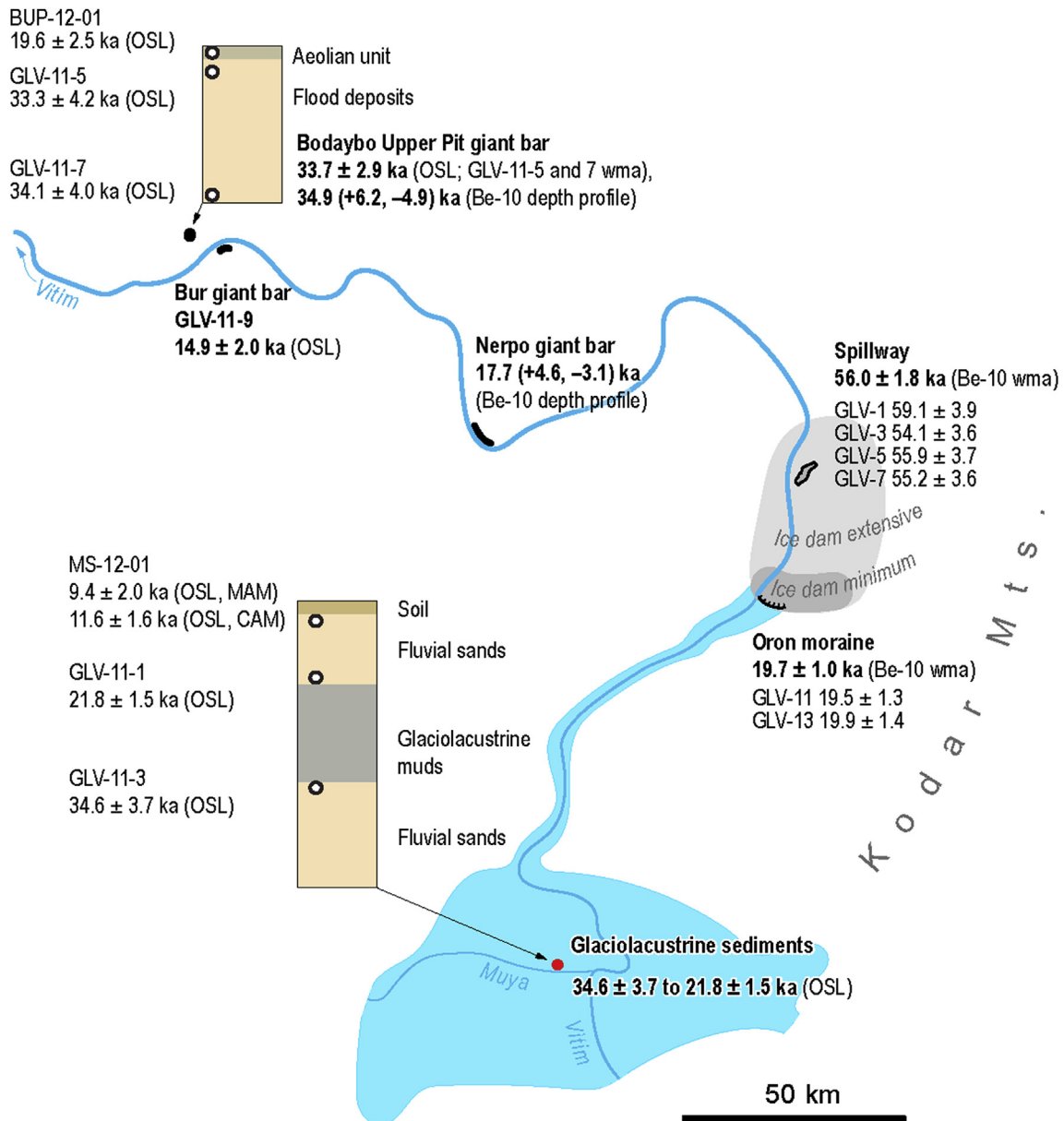


**Fig. 12. Summary of geochronology for glacial Lake Vitim and its floods.** Chronology is shown  $\pm 1\sigma$ , weighted mean ages (wma) are calculated for sites with multiple dates. See Table 2 for samples GLV-9 and GLV-15, which are not directly relevant for the reconstructed flood chronology.

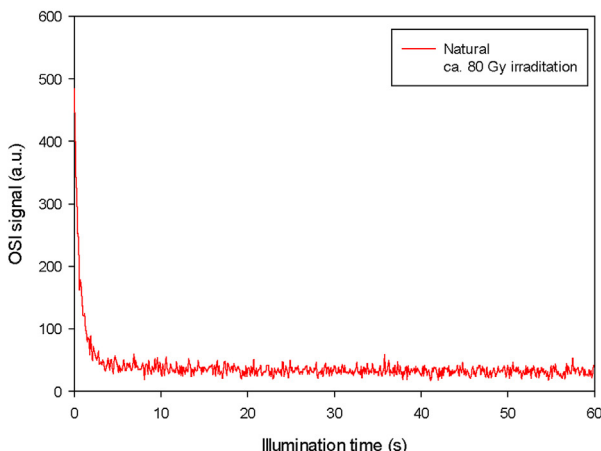
accommodated in our flood chronology: the large block ( $7 \times 7 \times 2$  m; Figs. 3 and 9) sampled midway down the talus slope in the bedrock spillway yielded an exposure age of  $24.7 \pm 1.7$  ka (Table 2), and another large talus block ( $6 \times 4 \times 2$  m) sampled on a bedrock island in the Oron delta (Fig. 3) yielded an exposure age of  $14.3 \pm 1.0$  ka (Table 2). We note that the talus block in the spillway falls just outside the  $1\sigma$  bounds with Flood III. Indeed, it is likely that some of the discharge of Flood III were routed through the spillway and might have caused erosion at the foot of its steep slopes. The age of the talus block in the Oron delta corresponds with the dating of a potential Late Glacial ice re-advance in the area (Margold et al., 2016) and, being just a few metres above the delta surface, possibly relates to glacial events further up-valley, such as ice calving into Lake Oron, or flooding at a smaller scale than the glacial Lake Vitim outbursts.

#### 4.3. Reconstructed peak discharge

##### 4.3.1. Peak discharge modelled with HEC-RAS

The minimum peak discharge accordant with the highest flood bars at Nerpo and Bur (dated to Flood-III, Fig. 15) is estimated at 4.0–6.5 million  $\text{m}^3/\text{s}$  assuming a plausible range of Manning's  $n$  (0.03–0.05; Tables 7 and 8). This stands as one of the largest freshwater floods ever documented on Earth (O'Connor and Costa, 2004). Our modelling predicts that the Vitim valley was flooded to depths of ~120–150 m (locally up to 200 m), with average flow velocities of up to  $21 \text{ m s}^{-1}$  (Table 8). By assuming a simple triangular flood hydrograph (Alho et al., 2010), based on the drainage volume and peak discharge, we estimate that Lake Vitim drained over a period of about 10–16 days. Flood-III was up to ~34-times larger than the most extreme historical floods on the Lena River associated with ice-jams (O'Connor and Costa, 2004). Owing to the

(a)



(b)

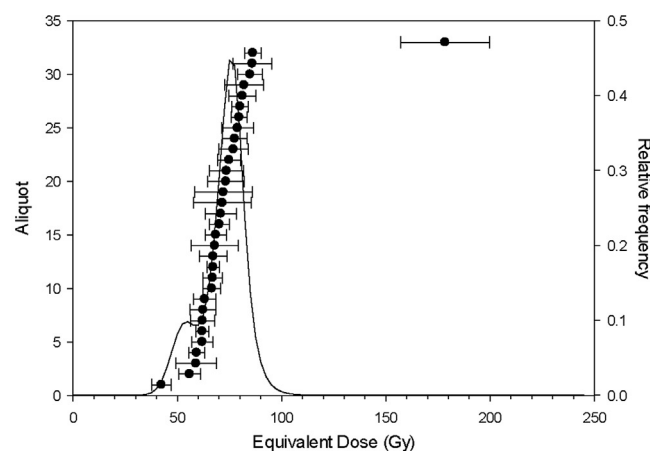


**Fig. 13. Optically stimulated luminescence (OSL) dating.** (a) Example of a natural and an artificial OSL decay curve of an aliquot of sample GLV-11-1. The almost identical shape indicates the absence of unstable signal components. (b) The spread of individual Equivalent Dose values for sample GLV-11-1 shows a narrow distribution around 80 Gy, which is interpreted to represent the aliquots that were zeroed at the time of deposition.

effects of flow storage, the heights of the giant eddy/expansion bars listed in Table 4 inevitably reflect some attenuation of the flood peak downstream of the breached ice-dam. Lower flood bars at Bodaybo and at the nearby town of Mamakan reflect flood discharges of no more than 1 million  $\text{m}^3/\text{s}$  and were presumably formed during the falling stages.

#### 4.3.2. Predicting peak flood discharge with empirical equations

In addition to modelling the flood propagation with HEC-RAS, we apply three simple empirical equations for estimating peak discharge ( $Q$ ) based on dimensions of the impoundment and the breach. Relevant parameters are:

$$V, \text{ total impoundment volume} = 3 \times 10^{12} \text{ m}^3;$$

$$D, \text{ maximum impoundment depth (below the shoreline at 840 m a.s.l.)} = 490 \text{ m};$$

$h$ , the change in impoundment level at the breach = 414 m (assuming that the bedrock spillway was the sole outflow point), or 490 m (assuming that the main Vitim valley was rapidly cleared of ice during the flood); and

**Table 5**  
Summary of Monte Carlo model parameters.

Site specific information	Nerpo	Bodaybo Upper	Bodaybo Lower
Latitude (decimal deg.)	57.521	57.922	57.922
Longitude (decimal deg.)	115.296	114.219	114.219
Altitude (m a.s.l.)	471	351	351
<b>Shielding</b>			
Topographic shielding	0.999	0.999	0.999
Cover	1	1	1
<b><math>^{10}\text{Be}</math> production rate (atoms/g/yr)</b>			
Spallation mean	6.39	5.72	5.72
Spallation standard dev.	0.35	0.32	0.32
<b>Bulk material density (g/cm<sup>3</sup>)</b>			
Mean	2.0	2.0	2.0
Standard deviation	0.2	0.2	0.2
<b>Monte Carlo parameters</b>			
Sigma confidence	3 <sup>a</sup>	2	2
Number of profiles	$10^5$	$10^5$	$10^5$
Min age (a)	5000	0	5000
Max age (a)	35000	40000	35000
Min erosion rate (cm/ka)	0	0	0
Max erosion rate (cm/ka)	5	10	5
Min total erosion threshold (cm)	0	0	0
Max total erosion threshold (cm)	50	50	50
Min inheritance (atoms g <sup>-1</sup> )	85000	50000	50000
Max inheritance (atoms g <sup>-1</sup> )	105000	175000	70000
Neutrons (min value)	150	150	150
Neutrons (max value)	160	160	160

<sup>a</sup> No solutions were found for 2-sigma confidence limit.

b, the breach width.

Following O'Connor and Beebe (2009), peak discharge from 'large' impoundments such as glacial Lake Vitim can be estimated by

$$Q \approx g^{0.5} h^{2.5}$$

where  $g$  is gravitational acceleration and  $h$  approximates the maximum specific energy at the outflow. The two different  $h$  values yield peak discharge estimates of 10.9 and 16.6 million  $\text{m}^3 \text{ s}^{-1}$ , where  $b/h \sim 1$ , but for wider breaches the estimates increase. An alternative, regression-derived function from moraine-dammed lakes is proposed by Cenderelli (2000):

$$Q \approx 0.3 (VD)^{0.49}$$

which yields peak discharge estimates of 7.5 and 8.1 million  $\text{m}^3 \text{ s}^{-1}$  (using  $D = 414$  and 490 m, respectively, as described above). A third regression-derived function from large-scale outburst floods ( $V > 1 \text{ km}^3$ ) is proposed by Herget (2005):

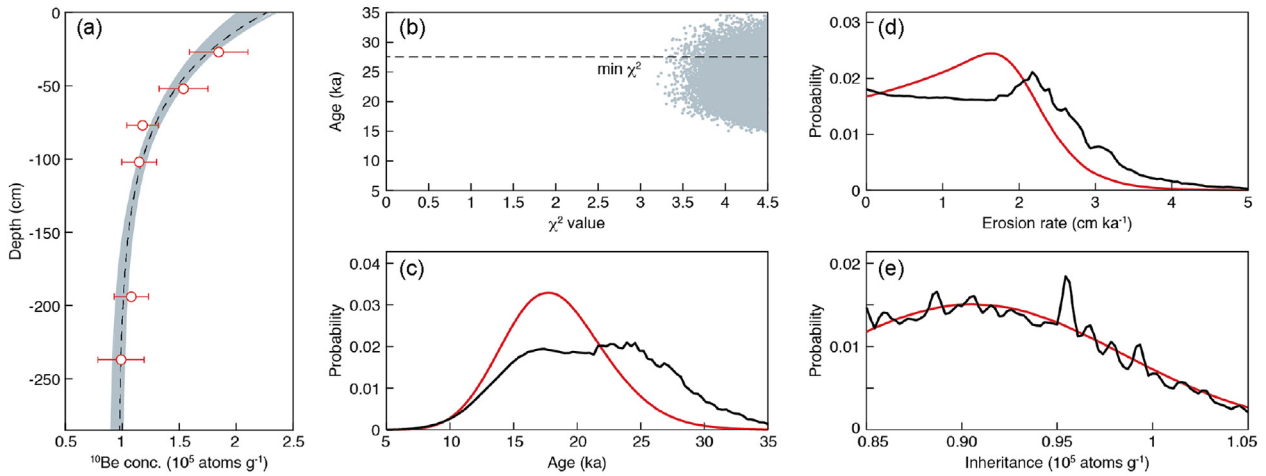
$$Q \approx 6645 V^{0.98}$$

and yields a peak discharge estimate of 17 million  $\text{m}^3 \text{ s}^{-1}$ . While acknowledging that we lack any information about the ice-dam breach, the range of peak discharges returned by the three simple empirical equations, 7.5–17 million  $\text{m}^3 \text{ s}^{-1}$ , is a similar order to that obtained from the HEC-RAS flood modelling and suggests that the latter may point to a conservative estimate.

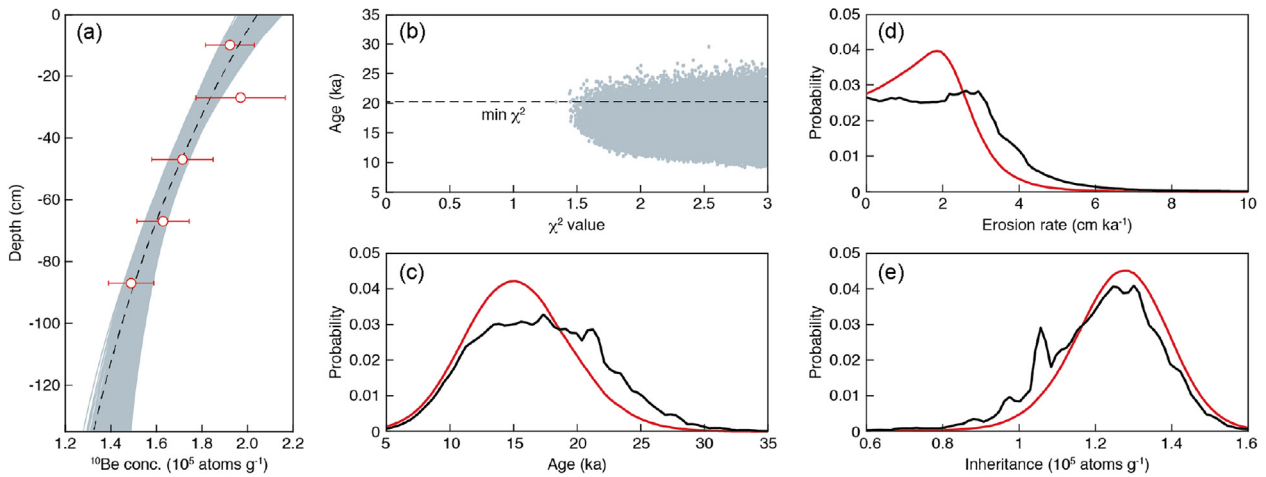
#### 4.4. Pre- and post-flood sedimentary environments of the Muya-Kuanda Depression

Sedimentary exposures in the Muya-Kuanda Depression reveal predominantly fluvial facies locally reworked at the surface into

## Nerpo



## Bodaybo 'Upper Pit' upper unit



## Bodaybo 'Upper Pit' lower unit

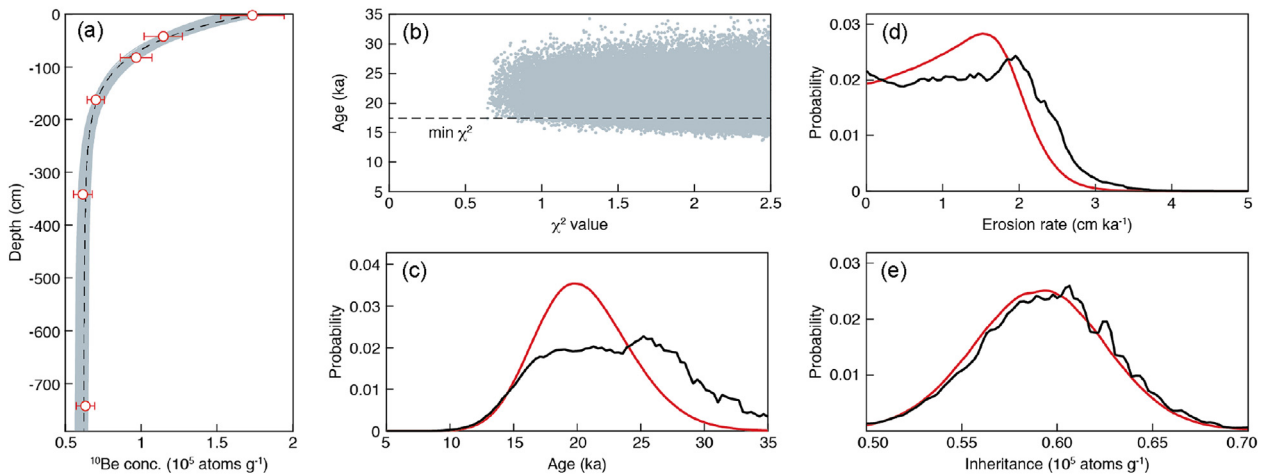


**Fig. 14. Age modelling from cosmogenic  $^{10}\text{Be}$  depth profiles at Nerpo and Bodaybo 'Upper Pit'.** (a) Cosmogenic  $^{10}\text{Be}$  depth profiles: red circles are measured  $^{10}\text{Be}$  concentrations (see Table 3); dashed black curve represents the theoretical depth profile with the lowest chi-squared fit to the data; grey shading comprises multiple curves representing all depth profiles fitting the  $^{10}\text{Be}$  data. Uncertainties are shown at  $3\sigma$  level for Nerpo and  $2\sigma$  level for Bodaybo 'Upper Pit' upper and lower units. Note that uncertainties for Nerpo  $^{10}\text{Be}$  concentrations are shown at  $3\sigma$  rather than  $2\sigma$  level because no solutions were found for this depth profile for a confidence limit  $< 3\sigma$ . (b) Age versus chi-squared plot for the depth profiles in (a). Dashed line shows age with minimum chi-squared value. (c) to (e) Smoothed chi-squared (black curves) and Bayesian probability density functions (red curves) for the depositional age, erosion rate, and  $^{10}\text{Be}$  inheritance of the Nerpo and Bodaybo units based on the  $^{10}\text{Be}$  depth profiles. All calculations performed using age calculator code of [Hidy et al. \(2010\)](#); version 1.2. See also Table 5 for details on model parameters used. (For interpretation of the references to colour in this figure legend, the reader is referred to the Web version of this article.)

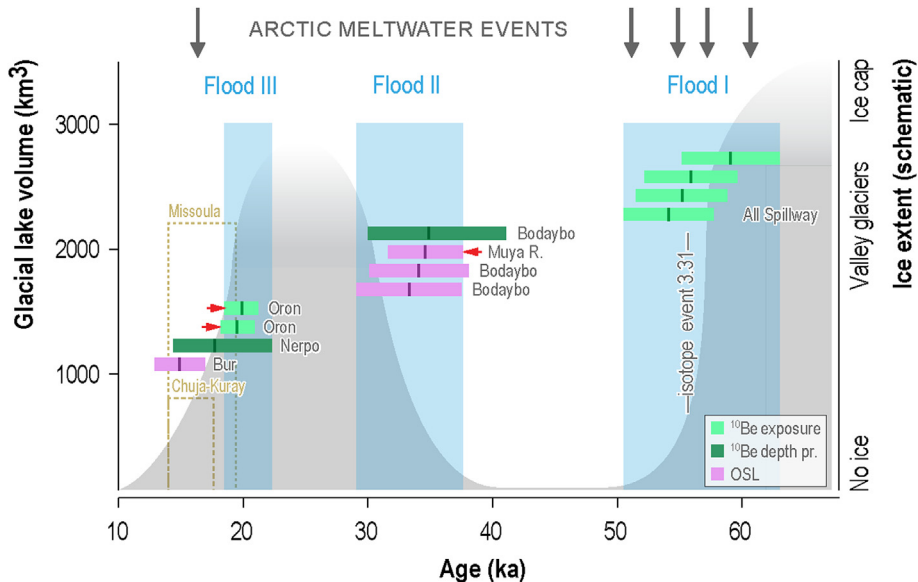


**Fig. 15. Outburst flood magnitude and chronology over the past 60 ka.** Flood volumes from Lake Vitim (blue columns), Lake Missoula (Baker et al., 2016; Gombiner et al., 2016) and Lake Chuja-Kuray (outlined brown columns; Herget, 2005). Note that only Flood-III was modelled directly; volumes shown for floods I and II are speculative, but shorelines at ~840 m a.s.l. match an overflow to the adjoining catchment and restrict glacial Lake Vitim's maximum volume to ~3000 km<sup>3</sup> (Margold et al., 2011). Schematic ice extent is shown in grey (Svendsen et al., 2004; Margold et al., 2016) along with Arctic meltwater events recorded in core PS2185 (Spielhagen et al., 2004). Chronology is shown via coloured error bands ( $\pm 1\sigma$ ) and limiting ages (red arrows; see the text and Fig. 12, Table 6 for more information). Age intervals of Vitim floods (blue columns) are defined by the span of  $1\sigma$  error bands. (For interpretation of the references to colour in this figure legend, the reader is referred to the Web version of this article.)

aeolian dunefields, now stabilised by vegetation. The Muya River is a sand-bed, meandering river with well-developed point-bars and numerous ~30 m high, concave-bank exposures formed where the eroding bank abuts fragments of a high alluvial terrace. The 11 m glaciolacustrine mud unit deposited by glacial Lake Vitim is located at one such terrace exposure. Sample MS-12-01 collected from 1.0 m below the top of the terrace section yields an OSL age of  $9.4 \pm 2.0$  ka and  $11.6 \pm 1.6$  ka using Minimum and Central age models (Galbraith et al., 1999), respectively (Figs. 5 and 12, Table 1). This indicates that the Muya River has incised ~30 m since ~11 ka, possibly in response to declining postglacial sediment supply. The Muya River floodplain contains well-developed ridge-and-swale topography, palaeochannel traces, oxbow lakes, and backplain swamps spanning a channel belt 1–2 km wide. Such landforms indicate that channel incision has been accompanied by considerable lateral channel migration over the Holocene. We surmise that active reworking of the valley fill may have removed part of the recent glaciolacustrine record of glacial Lake Vitim and, conversely, older (pre-Flood II) glaciolacustrine units presumably lie buried and unexposed. The vigour of Holocene sedimentary dynamics along the Muya and Vitim rivers may also explain the lack of clear evidence of abrupt lake-draining, such as fluvial sand and gravel dunes observed in glacial lake basins elsewhere (Waitt, 1980; Carling, 1996; Carling et al., 2009; Wiedmer et al., 2010).

The glaciolacustrine muds exposed in the Muya River section are bracketed by an OSL age of  $34.6 \pm 3.7$  ka (GLV-11-3; Fig. 12, Table 1) on fluvial sands just prior to Vitim-damming, and an OSL age of  $21.8 \pm 1.5$  ka (GLV-11-1; Fig. 12, Table 1) marking the local resumption of fluvial sedimentation some time later. Although we observed no internal breaks in glaciolacustrine sedimentation, we cannot exclude the possibility that the 11 m sequence spans both lake phases that preceded floods II and III (by comparison, an ice-dammed lake in the Chara Depression [~200 km north-east of the Muya-Kuanda Depression, Fig. 2] produced a 17 m stack of varved glaciolacustrine muds over ~1200 y [Enikeev, 1986]). This suggests a couple of possible scenarios: 1) the Muya River section hosts an

incomplete record of one or more lakes with an unidentified erosional break, or 2) post-flood fluvial sedimentation was displaced elsewhere in the Muya valley for possibly several thousand years, meaning that the OSL date of  $21.8 \pm 1.5$  ka is very much a minimum age of the return of fluvial conditions at the section we sampled.

## 5. Discussion

### 5.1. Correlation of the glacial Lake Vitim floods with sediments along the Lena River and in the Lena Delta

Although the downstream extent of our field investigations was limited to the Vitim confluence with its tributary Mamakan (Fig. 2), we identify possible traces of the Vitim megafloods in previous descriptions of fluvial landforms and sediments along the Lena River and in the Lena Delta. In the middle reaches of the Lena River just above the Aldan River junction, the Bestyakh Terrace (Fig. 10a) stands 15–73 m above the Lena River and up to 70 km wide (Kamaletdinov and Minjuk, 1991). The Lena here becomes considerably less laterally-confined; hence a megaflood would be expected to deposit its sediment load over a wide area. The terrace is composed of four units of which the Mavrian unit of parallel and cross-bedded sands is interpreted by previous workers (Kamaletdinov and Minjuk, 1991; Grinenko et al., 1995) as comprising reworked glaciolacustrine material from the Baikal-Patom Uplands (i.e., the Vitim River between the ice-dam site and the Lena confluence; Fig. 2). The Mavrian unit has been correlated to the Muorin unit in the Lena Delta (Galabala, 1987), later termed the Arga Complex (Schwamborn et al., 2002; Schirrmeyer et al., 2011).

As the Lena River nears the coast, it passes between the Chukanovsky and Kharaulakh mountain ridges, where the passage of extreme floods would be constricted from >50 km upstream to 2–10 km, focusing erosive power at the delta apex (Fig. 10b). We anticipate catastrophic erosion, avulsion of primary distributaries, and abrupt delta-lobe switching resulting in a mosaic of cut-and-fill

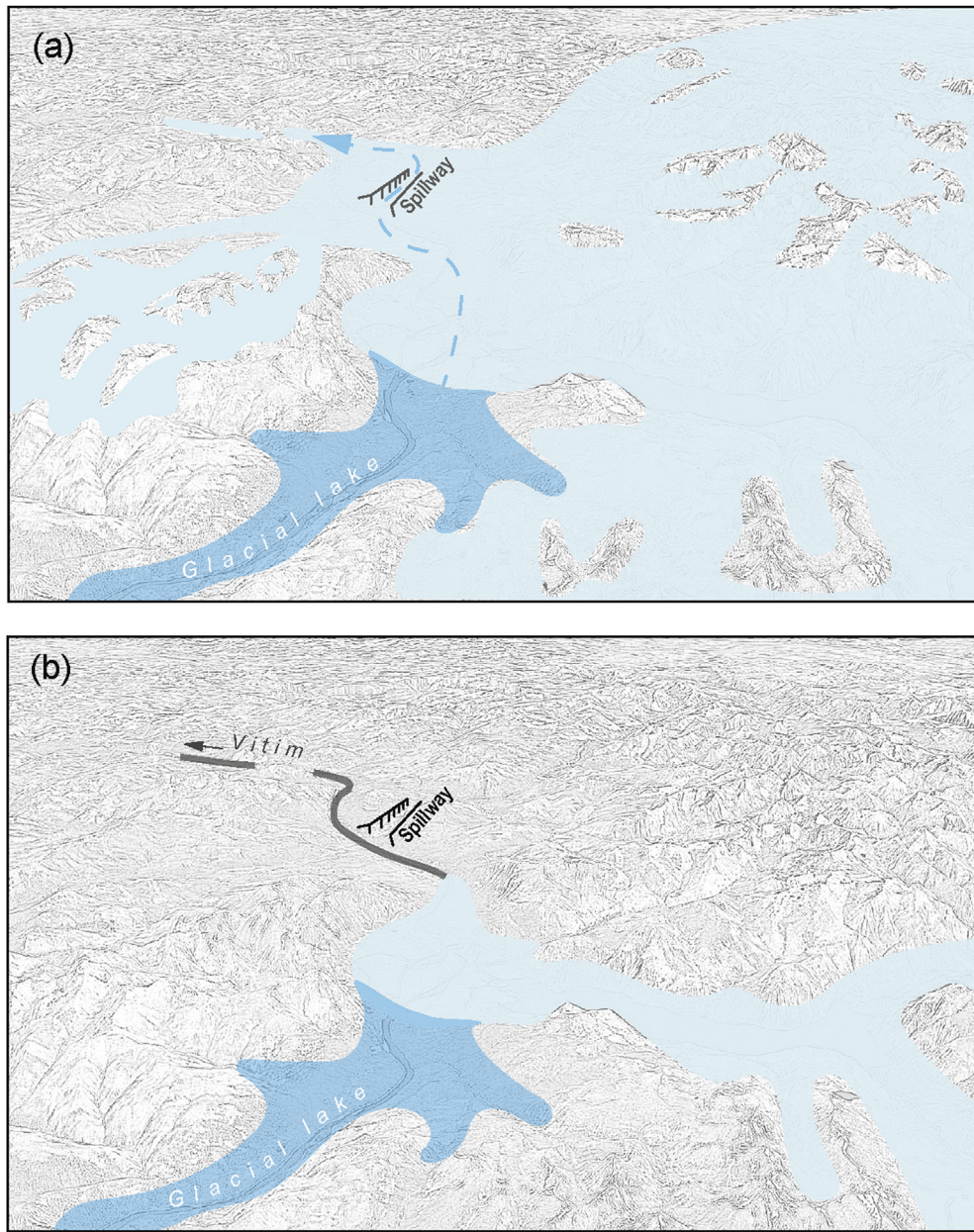


**Fig. 16. Hypothesised ice dam configurations.** Schematic depiction of two hypothesised configurations of the ice dam. (a) Vitim valley blocked by an ice cap covering the Kodar Mountains and burying the surrounding lower ground with ice. In this configuration, the Vitim valley was filled with ice for several tens of kilometres. Flood I (dashed blue line, though note we refrain from inferring the exact mechanism of the ice dam collapse), is inferred to have occurred under this ice-dam configuration. The regional glacial geomorphology indicates that at least one previous glaciation was even more extensive and most of the landscape visible here was covered by ice (Margold et al., 2016; see Fig. 2 here). (b) Vitim valley blocked by a single ice lobe emanating from the valley occupied at present by Lake Oron. In this configuration, the length of the ice dam was only a few kilometres and a minor retreat of the valley glacier would trigger release of the impounded glacial Lake Vitim; note spillway, which must have formed under more extensive ice cover, in background. (For interpretation of the references to colour in this figure legend, the reader is referred to the Web version of this article.)

across the delta. West of the active late Holocene-modern accumulation zone lie erosional remnants of two terraces: the Arga Complex and Ice Complex (Fig. 10b; Schwamborn et al., 2002; Schirrmeyer et al., 2011). The Arga Complex, correlated with the Bestyakh Terrace described above (Grinenko et al., 1995; Schirrmeyer et al., 2003, Fig. 10a), is noted as the thickest, most widespread sedimentary unit in the delta, comprising medium-grained, well-sorted, weakly bedded, and organic-free sands. Schirrmeyer et al. (2003) suggest that the massive sandy deposits "accumulated on the bottom and sides of large meltwater streams when large, extended areas of the periglacial plain were flooded in

the spring" (see also Schwamborn et al., 2002). The OSL chronology ascribes these sandy deposits to >100 ka to ~50 ka (Schirrmeyer et al., 2011). However, we propose that the high-energy deposits observed along the Lena's middle reaches and at the delta are consistent with the expected long-range effects of cataclysmic outburst floods from Lake Vitim. This suggestion finds support in the available chronology for the stratigraphy of the delta: the deposition of the lower Arga Complex (Schwamborn et al., 2002; Schirrmeyer et al., 2011) is coeval with Flood-I, and the timing of floods II and III matches erosion gaps in the Ice Complex (32–17 ka and 17–8 ka) at Kurungnakh-Sise Island (Wetterich et al., 2008), a

**Table 6**

List of floods &amp; available evidence.

Flood	Evidence	Dating	Relevant figures
1	Spillway	56.0 ± 1.8 ka ( $^{10}\text{Be}$ , this study)	2, 3, 4
	Bestyakh Terrace <sup>a,b</sup>	>100 ka to ~50 ka <sup>d</sup>	10a
	Arga Sands <sup>c,d</sup>		10b
2	Sand peak in core PS2741-1 <sup>e</sup>	55.5 ka <sup>g</sup>	15
	Isotope-event 3.31 <sup>f,g</sup>	34.6 ± 3.7 to 21.8 ± 1.5 ka (OSL, this study)	2, 5, 12
	Glacio-lacustrine sediments Muya River	33.7 ± 2.9 ka (OSL), 34.9 (+6.2, -4.9) ka ( $^{10}\text{Be}$ , this study)	2, 8, 12
3	Bodaybo 'Upper Pit' eddy bar		10a
	Bestyakh Terrace <sup>a,b</sup>	32–17 ka <sup>h</sup>	10b
	Erosion gap in Ice Complex (Lena Delta) <sup>h</sup>	19.7 ± 1.0 ka (Be-10) <sup>i</sup>	2, 3, 12
3	Oron moraine (must postdate Flood 3)	17.7 (+4.6, -3.1) ka (Be-10, this study)	2, 6, 12
	Eddy bar Nerpo	14.9 ± 2.0 ka (OSL, this study)	2, 7, 12
	Eddy bar Bur		2, 11
3	Undated giant bars		10a
	Bestyakh Terrace <sup>a,b</sup>		10b
	Erosion gap in Ice Complex (Lena Delta) <sup>h</sup>	17–8 ka <sup>h</sup>	

<sup>a</sup> Kamaletdinov and Minjuk (1991).<sup>b</sup> Galabala (1987).<sup>c</sup> Schwamborn et al. (2002).<sup>d</sup> Schirrmeister et al. (2011).<sup>e</sup> Knies et al. (2000).<sup>f</sup> Nørgaard-Pedersen et al. (1998).<sup>g</sup> Martinson, et al. (1987).<sup>h</sup> Wetterich, et al. (2008).<sup>i</sup> Margold et al. (2016).**Table 7**Predicted minimum peak discharge for Flood-III using different Manning's *n*.

Bar type & position	Minimum peak discharge <sup>a</sup>		
	$\times 10^6 \text{ m}^3 \text{ s}^{-1}$	$n = 0.03$	$n = 0.04$
Eddy bar at Nerpo	5.5	4.5	4.0
Eddy bar complex at Bur (crest)	6.5	5.0	4.5

<sup>a</sup> Discharge (rounded to nearest 0.5 million  $\text{m}^3 \text{ s}^{-1}$ ) at which giant eddy bars are submerged.

site especially vulnerable to megaflood erosion (Fig. 10b).

## 5.2. Megaflood traces in Arctic Ocean sediment cores

A large meltwater influx to the Arctic Ocean marks the penultimate deglaciation at ~57–52 ka (Nørgaard-Pedersen et al., 1998; Spielhagen et al., 2004; Stein, 2008). Drainage of glacial lakes from the Eurasian ice sheet is cited as the meltwater source (Fig. 1; Mangerud et al., 2004; Spielhagen et al., 2004), although details of volume and timing remain unresolved. The most pronounced meltwater pulse, labelled isotope event 3.31 at 55.5 ka (Martinson et al., 1987; Nørgaard-Pedersen et al., 1998), is identified in circum-Arctic cores via peaks in isotopic freshwater indicators and ice-rafted debris (Martinson et al., 1987; Nørgaard-Pedersen et al., 1998). At the continental margin north-west of the Laptev Sea (core PS2741-1; Fig. 1), close to where the Lena River met the former coast at lower sea-level, isotope event 3.31 is shown to be the most prominent peak in the sand fraction throughout the entire

core length—significantly more pronounced than Termination II, although comparable after accounting for ice rafted debris (Knies et al., 2000; Stein, 2008). Our Flood I is dated by the incision of the bedrock spillway to  $56.0 \pm 1.8$  ka. The coincident timing and the sedimentary signature lead us to connect Flood-I with event 3.31, although it is likely that deglaciation from OIS-4 released multiple coeval meltwater sources around the Arctic (Mangerud et al., 2004; Stein, 2008). Accounting for some bedrock surface weathering on the spillway, the weighted mean surface exposure ages for Flood-I range between  $56.5 \pm 1.9$  and  $61.8 \pm 2.3$  ka (see Section 4.1.2.), which is still within  $1\sigma$  uncertainty of the timing of isotope event 3.31 ( $55.5 \pm 5$  ka; Martinson et al., 1987).

## 5.3. Possible climate implications of cataclysmic glacial outburst floods

Abrupt meltwater influx to the Arctic Ocean can have important implications for climate. Much attention has been directed at freshwater influx disruption to the Atlantic Meridional Overturning Circulation (AMOC) during the last deglaciation (Broecker et al., 1989; Barber et al., 1999; Condron and Winsor, 2012), but the impact of similar events prior to OIS-2 has not drawn a similar level of interest (Oppo and Lehman, 1995), as so little is known of these older episodes. Massive pre-OIS-2 outbursts from Eurasia produced Arctic freshwater pulses that the Transpolar Drift (Fig. 1) could have conveyed to regions critical for AMOC perturbation (Condron and Winsor, 2012). Indeed, modelling experiments indicate that the AMOC is highly sensitive to freshwater export from the Arctic Ocean (Rennermalm et al., 2006; Zhang et al., 2014). While the

**Table 8**Predicted flood variables for Flood-III using different Manning's *n*.

Flood variable	$n = 0.03$	$n = 0.04$	$n = 0.05$
Average flow velocity <sup>a</sup> ( $\text{m s}^{-1}$ )	11–17 (21)	12–17 (21)	8–12 (14)
Average Froude number <sup>a</sup>	0.29–0.45 (0.54)	0.33–0.50 (0.61)	0.21–0.30 (0.36)
Average shear stress <sup>a</sup> ( $\text{N m}^{-2}$ )	212–485 (717)	165–373 (566)	294–615 (916)
Average hydraulic depth <sup>a</sup> (m)	135–169 (193)	110–139 (159)	138–167 (189)
Average top flow width <sup>a</sup> (m)	4992–2102	2046–4286	2036–5079

<sup>a</sup> Averaged for total cross-sections given as 1-sigma range, with maximum value in parentheses.

floods documented here for glacial Lake Vitim likely did not have sufficient volume to cause hemispheric-wide impact on climate, influx of water from the lakes dammed by the Eurasian Ice Sheet could possibly have triggered climate feedbacks as with North American meltwater discharges during the last deglaciation (Broecker et al., 1989; Barber et al., 1999). The climate dynamics underlying the OIS-4–3 transition (Rasmussen et al., 2014) stands as a prime candidate for further investigation.

## 6. Conclusions

We reconstruct cataclysmic outburst floods from glacial Lake Vitim in Siberia that followed the Vitim and Lena rivers into the Arctic Ocean. Using a combination of  $^{10}\text{Be}$  exposure dating and OSL, we establish a chronology for these floods that distinguishes three flood events over the past 60,000 years. The timing of the floods is consistent with the regional glacial history: Flood I occurred during deglaciation following OIS-4 and its timing at ~56 ka is coincident with isotope event 3.31 documented in Arctic Ocean sediment cores; Flood-II occurred during the build-up to the local Last Glacial Maximum; and Flood-III during the last deglaciation. The glacial Lake Vitim outbursts are among the largest freshwater floods ever documented. We estimate the peak discharge of Flood-III using the HEC-RAS model at 4.0–6.5 million  $\text{m}^3\text{s}^{-1}$ , with mean flow depths of 120–150 m and average flow velocities up to 21  $\text{m s}^{-1}$ . These results offer a new record of outburst floods spanning OIS-3 and 2, and one of the largest megaflood discharges for which timing and geomorphic impacts are well resolved.

## Acknowledgments

We thank Anton Brichevskiy for partaking in fieldwork, Larisa Chechetkina and staff of the Vitim Nature Reserve for logistical support, and Charles Mifsud and Steven Kotevski for their assistance with measurement of  $^{10}\text{Be}$  samples at ANSTO. This research was funded by the Swedish Society for Anthropology and Geography, the Bolin Centre for Climate Research, the Royal Swedish Academy of Sciences (FOA12Althin- 034), Stockholm University, and Stiftelse YMER-80 to Martin Margold; and by the Australian Institute of Nuclear Science and Engineering (ALNGRA12021P), the Australian Research Council (DP130104023), and a Marie Skłodowska-Curie fellowship to John Jansen. We heartily thank Victor Baker, Paul Carling, Tim Cohen, Jürgen Herget, Oliver Korup, Wolfgang Schwanghart, and Chris Stokes for comments on early drafts of the manuscript. We thank two anonymous reviewers who provided constructive comments on the submitted version of the manuscript.

## References

Alho, P., Baker, V.R., Smith, L.N., 2010. Paleohydraulic reconstruction of the largest Glacial Lake Missoula draining(s). *Quat. Sci. Rev.* 29, 3067–3078.

André, M.-F., 2002. Rates of postglacial rock weathering on glacially scoured outcrops (Abisko-Riksgränsen area, 68° N). *Geogr. Ann.: Phys. Geogr.* 84, 139–150.

Baker, V.R., 2001. Water and the martian landscape. *Nature* 412, 228–236.

Baker, V.R., Benito, G., Rudoy, A.N., 1993. Paleohydrology of late Pleistocene super-flooding, Altay mountains, Siberia. *Science* 259, 348–350.

Baker, V.R., Bjornstad, B.N., Gaylord, D.R., Smith, G.A., Meyer, S.E., Alho, P., Breckenridge, R.M., Sweeney, M.R., Zreda, M., 2016. Pleistocene megaflood landscapes of the channelled Scabland. In: Lewis, R.S., Schmidt, K.L. (Eds.), *Exploring the Geology of the Inland Northwest*. Geological Society of America Field Guide, vol 41, pp. 1–73.

Baker, V.R., Bunker, R.C., 1985. Cataclysmic late Pleistocene flooding from glacial Lake Missoula: a review. *Quat. Sci. Rev.* 4, 1–41.

Balco, G., Stone, J.O., Lifton, N.A., Dunai, T.J., 2008. A complete and easily accessible means of calculating surface exposure ages or erosion rates from  $^{10}\text{Be}$  and  $^{26}\text{Al}$  measurements. *Quat. Geochronol.* 3, 174–195.

Barber, D.C., Dyke, A., Hillaire-Marcel, C., Jennings, A.E., Andrews, J.T., Kerwin, M.W., Bilodeau, G., McNeely, R., Southon, J., Morehead, M.D., Gagnon, J.M., 1999. Forcing of the cold event of 8,200 years ago by catastrophic drainage of Laurentide lakes. *Nature* 400, 344–348.

Batbaatar, J., Gillespie, A.R., 2016a. Outburst floods of the Maly Yenisei. Part I. *Int. Geol. Rev.* 58, 1723–1752.

Batbaatar, J., Gillespie, A.R., 2016b. Outburst floods of the Maly Yenisei. Part II—new age constraints from Darhad basin. *Int. Geol. Rev.* 58, 1753–1779.

Bazarov, D.B., 1986. *The Cenozoic of Cisbaikalia and Western Transbaikalia*. Nauka, Novosibirsk (in Russian).

Bazarov, D.B., Rezanov, I.N., Budava, R.C., Imethenov, A.B., et al., 1981. *The Geomorphology of Northern Cisbaikalia and the Stanovoe Range*. Nauka, Moscow (in Russian).

Bjornstad, B.N., Fecht, K.R., Pluhar, C.J., 2001. Long history of pre-Wisconsin, ice age cataclysmic floods: evidence from southeastern Washington state. *J. Geol.* 109, 695–713.

Bohorquez, P., Carling, P.A., Herget, J., 2016. Dynamic simulation of catastrophic late Pleistocene glacial-lake drainage, Altai Mountains, central Asia. *Int. Geol. Rev.* 58, 1795–1817.

Borchers, B., Marrero, S., Balco, G., Caffee, M., Goehrung, B., Lifton, N., Nishiizumi, K., Phillips, F., Schaefer, J., Stone, J., 2016. Geological calibration of spallation production rates in the CRONUS-Earth project. *Quat. Geochronol.* 31, 188–198.

Broecker, W.S., Kennett, J.P., Flower, B.P., Teller, J.T., Trumbore, S., Bonani, G., Wolfli, W., 1989. Routing of meltwater from the Laurentide Ice Sheet during the Younger Dryas cold episode. *Nature* 341, 318–321.

Carling, P.A., 1996. Morphology, sedimentology and palaeohydraulic significance of large gravel dunes, Altai Mountains, Siberia. *Sedimentology* 43, 647–664.

Carling, P.A., 2013. Freshwater megaflood sedimentation: what can we learn about generic processes? *Earth Sci. Rev.* 125, 87–113.

Carling, P.A., Kidson, R., Cao, Z., Herget, J., 2003. Palaeohydraulics of extreme flood events: reality and myth. In: Gregory, K.J., Benito, G. (Eds.), *Palaeohydrology: Understanding Global Change*. Wiley, pp. 325–336.

Carling, P.A., Kirkbride, A.D., Parnachov, S., Borodavko, P.S., Berger, G.W., 2009. Late quaternary catastrophic flooding in the Altai mountains of south-central Siberia: a synoptic overview and an introduction to flood deposit sedimentology, flood and megaflood processes and deposits. In: Martini, I.P., Baker, V.R., Garzon, G. (Eds.), *Flood and Megaflood Processes and Deposits*. Blackwell Publishing, pp. 17–35.

Carling, P., Villanueva, I., Herget, J., Wright, N., Borodavko, P., Morvan, H., 2010. Unsteady 1D and 2D hydraulic models with ice dam break for Quaternary megaflood, Altai Mountains, southern Siberia. *Global Planet. Change* 70, 24–34.

Cenderelli, D.A., 2000. Floods from natural and artificial dam failures. In: Wohl, E.E. (Ed.), *Inland Flood Hazards: Human, Riparian and Aquatic Communities*. Cambridge University Press, Cambridge, pp. 73–103.

Child, D., Elliott, G., Mifsud, C., Smith, A.M., Fink, D., 2000. Sample processing for earth science studies at ANTARES. *Nucl. Instrum. Methods Phys. Res. Sect. B Beam Interact. Mater. Atoms* 172, 856–860.

Chmeleff, J., von Blanckenburg, F., Kossett, K., Jakob, D., 2010. Determination of the  $^{10}\text{Be}$  half-life by multicollector ICP-MS and liquid scintillation counting. *Nucl. Instrum. Methods Phys. Res. Sect. B Beam Interact. Mater. Atoms* 268, 192–199.

Condron, A., Winsor, P., 2012. Meltwater routing and the younger dryas. *Proc. Natl. Acad. Sci. United States Am.* 109, 19928–19933.

Dewald, A., Heinze, S., Jolie, J., Zilges, A., Dunai, T., Rethemeyer, J., Melles, M., Staubwasser, M., Kuczewski, B., Richter, J., Radtke, U., 2013. CologneAMS, a dedicated center for accelerator mass spectrometry in Germany. *Nucl. Instrum. Methods Phys. Res. Sect. B Beam Interact. Mater. Atoms* 294, 18–23.

Enikeev, F.I., 1986. Sedimentation in Chara basin in late Pleistocene and Holocene. In: Sarin, L.P. (Ed.), *Problems of Geology and Metallogeny of the Chita Region*. RSFSR Mingeo, Moscow, pp. 37–43 (In Russian).

Enikeev, F.I., 2008. The late cenozoic of northern Transbaikalia and paleoclimates of southern east Siberia. *Russ. Geol. Geophys.* 49, 602–610.

Enikeev, F.I., 2009. Pleistocene glaciations in the east Transbaikalia and the south-east of middle Siberia. *Geomorfologiya* 40, 33–49 (In Russian).

Environmental Systems Research Institute, 2011. *ArcGIS 10.2 for Desktop*. California, Redlands.

Fink, D., Smith, A., 2007. An inter-comparison of  $^{10}\text{Be}$  and  $^{26}\text{Al}$  AMS reference standards and the  $^{10}\text{Be}$  half-life. *Nucl. Instrum. Methods Phys. Res. Sect. B Beam Interact. Mater. Atoms* 259, 600–609.

Galabala, R.O., 1987. New data for the structure of the Lena delta. In: Pohnalaynen, V.P. (Ed.), *Quaternary Period of Northeastern Asia*. SVKNII DVO AN SSSR, Magadan, pp. 152–171 (In Russian).

Galbraith, R.F., Roberts, R.G., Laslett, G.M., Yoshida, H., Olley, J.M., 1999. Optical dating of single and multiple grains of quartz from Jimiun rock shelter, northern Australia: Part I, experimental design and statistical models. *Archaeometry* 41, 339–364.

Gombiner, J.H., Hemming, S.R., Hendy, I.L., Bryce, J.G., Blichert-Toft, J., 2016. Isotopic and elemental evidence for Scabland flood sediments offshore Vancouver Island. *Quat. Sci. Rev.* 139, 129–137.

Grinenko, V.S., Kameletdinov, V.A., Slastenov, Y.L., Shcherbakov, O.I., 1995. Geological structure of Greater Yakutia. In: Slastenov, Y.L., Melcer, M.L., Fridoeskiy, V.Y. (Eds.), *Regional Geology of Yakutia*. Yakutian State University, Yakutsk, pp. 3–20 (In Russian).

Grosswald, M.G., Rudoy, A.N., 1996. Quaternary glacier-dammed lakes in the mountains of Siberia. *Polar Geogr.* 20, 180–198.

Heisinger, B., Lal, D., Jull, A.J.T., Kubik, P., Ivy-Ochs, S., Neumaier, S., Knie, K., Lazarev, V., Nolte, E., 2002a. Production of selected cosmogenic radionuclides by muons: 1. Fast muons. *Earth Planet. Sci. Lett.* 200, 345–355.

Heisinger, B., Lal, D., Jull, A.J.T., Kubik, P., Ivy-Ochs, S., Knie, K., Nolte, E., 2002b. Production of selected cosmogenic radionuclides by muons: 2. Capture of negative muons. *Earth Planet. Sci. Lett.* 200, 357–369.

Herget, J., 2005. Reconstruction of Pleistocene ice-dammed lake outburst floods in the Altai mountains, Siberia. *Geol. Soc. Am. Spec. Pap.* 386, 1–118.

Heyman, J., 2014. Paleoglaciation of the Tibetan Plateau and surrounding mountains based on exposure ages and ELA depression estimates. *Quat. Sci. Rev.* 91, 30–41.

Hide, A.J., Gosse, J.C., Pederson, J.L., Mattern, J.P., Finkel, R.C., 2010. A geologically constrained Monte Carlo approach to modeling exposure ages from profiles of cosmogenic nuclides: an example from Lees Ferry, Arizona. *Geochem. Geophys. Geosystems* 11, Q00A10.

Hydrologic Engineering Center, 2010. HEC-RAS, River Analysis System Version 4.1.0. United States Army Corps of Engineers, Davis, California.

Hydrologic Engineering Center, 2011. HEC-GeoRAS Version 10.1. United States Army Corps of Engineers, Davis, California.

Kamaletdinov, V.A., Minjuk, P.S., 1991. Composition and characteristics of Bestyakh terrace in the middle reaches of Lena. *Bull. Comm. Stud. Quat.* 60, 69–78 (In Russian).

Knies, J., Nowaczyk, N., Müller, C., Vogt, C., Stein, R., 2000. A multiproxy approach to reconstruct the environmental changes along the Eurasian continental margin over the last 150 000 years. *Mar. Geol.* 163, 317–344.

Kohl, C.P., Nishiizumi, K., 1992. Chemical isolation of quartz for measurement of in-situ-produced cosmogenic nuclides. *Geochim. Cosmochim. Acta* 56, 3583–3587.

Kolometyi, V.L., 2008. Paleogeography and Quaternary terrace sediments and complexes, intermontane basins of Prebaikalia (Southeastern Siberia, Russia). *Quat. Int.* 179, 58–63.

Komatsu, G., Arzhannikov, S.G., Gillespie, A.R., Burke, R.M., Miyamoto, H., Baker, V.R., 2009. Quaternary paleolake formation and cataclysmic flooding along the upper Yenisei River. *Geomorphology* 104, 143–164.

Komatsu, G., Baker, V.R., Arzhannikov, S.G., Gallagher, R., Arzhannikova, A.V., Murana, A., Oguchi, T., 2016. Catastrophic flooding, palaeolakes, and late Quaternary drainage reorganization in northern Eurasia. *Int. Geol. Rev.* 58, 1693–1722.

Korschinek, G., Bergmaier, A., Faestermann, T., Gerstmann, U.C., Knie, K., Rugel, G., Wallner, A., Dillmann, I., Dollinger, G., Von Gostomski, C.L., Kossert, K., 2010. A new value for the half-life of  $^{10}\text{Be}$  by heavy-ion elastic recoil detection and liquid scintillation counting. *Nucl. Instrum. Methods Phys. Res. Sect. B Beam Interact. Mater. Atoms* 268, 187–191.

Korup, O., Tweed, F., 2007. Ice, moraine, and landslide dams in mountainous terrain. *Quat. Sci. Rev.* 26, 3406–3422.

Krivenogov, S.K., Safonova, I.Y., 2017. Basin structures and sediment accumulation in the Baikal Rift zone: implications for cenozoic intracontinental processes in the central Asian orogenic belt. *Gondwana Res.* 47, 267–290.

Krivenogov, S.K., Takahara, H., 2003. Late pleistocene and holocene environmental changes recorded in the terrestrial sediments and landforms of eastern Siberia and North Mongolia. In: Kamata, N. (Ed.), *Proceedings of International Symposium of the Kanazawa University 21st-Century COE Program*, vol. 1, pp. 30–36.

Kulchitskiy, A.A., Panychev, V.A., Orlova, L.A., 1990. Late Pleistocene deposits of the Muya-Kuanda depression and their rate of accumulation. In: 7th Union Conference on Quaternary Research "Quaternary Period: Research Methods, Stratigraphy and Ecology", pp. 112–113. Tallin. (In Russian).

Kulchitskiy, A.A., Pulyavskiy, G.M., 1988. Evidence of catastrophic rise in the water level in the Holocene within the Muya depression. In: Laperdin, V.K., Altukhov, E.N. (Eds.), *Applied Geomorphology and Neotectonics of the South of Eastern Siberia*. Institute of the Earth's crust, Siberian Branch of the Academy of Sciences of the USSR, Irkutsk (In Russian).

Kulchitskiy, A.A., Skovitina, T.M., Ufimtsev, G.F., 1995. The ability to quickly flood the bottom of the Muya basin by a collapsing ravine in the Parama Canyon of the Vitim. In: *Environmental Aspects of Theoretical and Applied Geomorphology: Proceedings of the International Conference "III Shchukin Reading"*, pp. 136–137 (In Russian).

Larsen, I.J., Lamb, M.P., 2016. Progressive incision of the Channeled Scablands by outburst floods. *Nature* 538, 229–232.

Mangerud, J., Jakobsson, M., Alexanderson, H., Astakhov, V., Clarke, G.K., Henriksen, M., Hjort, C., Krinner, G., Lunkka, J.P., Möller, P., Murray, A., 2004. Ice-dammed lakes and rerouting of the drainage of northern Eurasia during the Last Glaciation. *Quat. Sci. Rev.* 23, 1313–1332.

Margold, M., Jansson, K.N., 2011. Glacial geomorphology and glacial lakes of central Transbaikalia, Siberia, Russia. *J. Maps* 7, 18–30.

Margold, M., Jansen, J.D., Gurinov, A.I., Codilean, A.T., Fink, D., Preusser, F., Reznichenko, N.V., Mifsud, C., 2016. Extensive glaciation in Transbaikalia, Siberia, at the Last Glacial Maximum. *Quat. Sci. Rev.* 132, 161–174.

Margold, M., Jansson, K.N., Stroeven, A.P., Jansen, J.D., 2011. glacial Lake Vitim, a 3000-km<sup>3</sup> outburst flood from Siberia to the Arctic Ocean. *Quat. Res.* 76, 393–396.

Martinson, D.G., Pisias, N.G., Hays, J.D., Imbrie, J., Moore Jr., T.C., Shackleton, N.J., 1987. Age dating and the orbital theory of the ice ages: development of a high-resolution 0 to 300,000-year chronostratigraphy. *Quat. Res.* 27, 1–29.

Mifsud, C., Fujioka, T., Fink, D., 2013. Extraction and purification of quartz in rock using hot phosphoric acid for in situ cosmogenic exposure dating. *Nucl. Instrum. Methods Phys. Res. Sect. B Beam Interact. Mater. Atoms* 294, 203–207.

Murray, A.S., Wintle, A.G., 2000. Luminescence dating of quartz using an improved single-aliquot regenerative-dose protocol. *Radiat. Meas.* 32, 57–73.

Nishiizumi, K., Imamura, M., Caffee, M.W., Southon, J.R., Finkel, R.C., McAninch, J., 2007. Absolute calibration of  $^{10}\text{Be}$  AMS standards. *Nucl. Instrum. Methods Phys. Res. Sect. B Beam Interact. Mater. Atoms* 258, 403–413.

Nørgaard-Pedersen, N., Spielhagen, R.F., Thiede, J., Kassens, H., 1998. Central Arctic surface ocean environment during the past 80,000 years. *Paleoceanography* 13, 193–204.

Obrechev, V.A., 1929. On the glaciation of the central Vitim mountain region. *Geogr. Bull.* 6, 42–45 (In Russian).

O'Connor, J., Beebee, R.A., 2009. 8 Floods from natural rock-material dams. In: Burr, D.M., Carling, P.A., Baker, V.R. (Eds.), *Megaflooding on Earth and Mars*. Cambridge University Press, Cambridge, pp. 128–163.

O'Connor, J.E., Costa, J.E., 2004. The World's Largest Floods, Past and Present: Their Causes and Magnitudes. US Geological Survey Circular 1254.

Oppo, D.W., Lehman, S.J., 1995. Suborbital timescale variability of north Atlantic deep water during the past 200,000 years. *Paleoceanography* 10, 901–910.

Osadchiy, S.S., 1979. Limno-glacial conditions and the issues of correlation of the Pleistocene formations in the depressions of the Stanovoe Highlands, the history of lakes in the USSR in the late Cenozoic. In: *Materials for the 5th All-union Symposium, Part 2 (Central Siberia, Cisbaikalia, Transbaikalia, Yakutia, the Far East)*, pp. 122–126. Irkutsk. (In Russian).

Osadchiy, S.S., 1982. On the Problem of the Relation of Glacial and Fluvial Epochs on the Territory of Northern Transbaikalia, Late Cenozoic History of Lakes in the USSR. Nauka, Novosibirsk (In Russian).

Petit, C., Déverchère, J., 2006. Structure and evolution of the Baikal rift: a synthesis. *Geochem. Geophys. Geosystems* 7, Q11016.

Preusser, F., Kasper, H.U., 2001. Comparison of dose rate determination using high-resolution gamma spectrometry and inductively coupled plasma-mass spectrometry. *Ancient TL* 19, 19–23.

Rasmussen, S.O., Bigler, M., Blockley, S.P., Blunier, T., Buchardt, S.L., Clausen, H.B., Cvijanovic, I., Dahl-Jensen, D., Johnsen, S.J., Fischer, H., Gkinis, V., Guillecic, M., Hoek, W.Z., Lowe, J.J., Pedro, J.B., Popp, T., Seierstad, I.K., Steffensen, J.P., Svensson, A.M., Vallelonga, P., Vinther, B.M., Walker, M.J.C., Wheatley, J.J., Winstrup, M., 2014. A stratigraphic framework for abrupt climatic changes during the Last Glacial period based on three synchronized Greenland ice-core records: refining and extending the INTIMATE event stratigraphy. *Quat. Sci. Rev.* 106, 14–28.

Rennermalm, A.K., Wood, E.F., Déry, S.J., Weaver, A.J., Eby, M., 2006. Sensitivity of the thermohaline circulation to Arctic Ocean runoff. *Geophys. Res. Lett.* 33, L12703.

Reuther, A.U., Herget, J., Ivy-Ochs, S., Borodavko, P., Kubik, P.W., Heine, K., 2006. Constraining the timing of the most recent cataclysmic flood event from ice-dammed lakes in the Russian Altai Mountains, Siberia, using cosmogenic in situ  $^{10}\text{Be}$ . *Geology* 34, 913–916.

Rytsk, E.Yu., Kovach, V.P., Yarmolyuk, V.V., Kovalenko, V.I., Bogomolov, E.S., Kotov, A.B., 2011. Isotopic structure and evolution of the continental crust in the east transbaikalian segment of the central Asian foldbelt. *Geotectonics* 45, 349–377.

Schirrmeister, L., Grosse, G., Schnelle, M., Fuchs, M., Krbetschek, M., Ulrich, M., Kunitsky, V., Grigoriev, M., Andreev, A., Kienast, F., Meyer, H., Babiy, O., Klimova, I., Bobrov, A., Wetterich, S., Schwamborn, G., 2011. Late quaternary paleoenvironmental records from the western Lena delta, Arctic Siberia. *Palaeogeogr. Palaeoclimatol. Palaeoecol.* 299, 175–196.

Schirrmeister, L., Grosse, G., Schwamborn, G., Andreev, A., Meyer, H., Kunitsky, V.V., Kuznetsova, T.V., Dorozhkin, M., Pavlova, E., Bobrov, A., 2003. Late Quaternary history of the accumulation plain north of the Chekanovsky Ridge (Lena Delta, Russia): a multidisciplinary approach. *Polar Geogr.* 27, 277–319.

Schwamborn, G., Rachold, V., Grigoriev, M.N., 2002. Late quaternary sedimentation history of the Lena delta. *Quat. Int.* 89, 119–134.

Spielhagen, R., Baumann, K.H., Erlenkeuser, H., Nowaczyk, N.R., Nørgaard-Pedersen, N., Vogt, C., Weiel, D., 2004. Arctic Ocean deep-sea record of northern Eurasian ice sheet history. *Quat. Sci. Rev.* 23, 1455–1483.

Steffen, D., Preusser, F., Schlunegger, F., 2009. OSL quartz age underestimation due to unstable signal components. *Quat. Geochronol.* 4, 353–362.

Stein, R., 2008. Chapter six quaternary variability of palaeoenvironment and its sedimentary record. In: Stein, R. (Ed.), *Arctic Ocean Sediments: Processes, Proxies, and Palaeoenvironment*. Elsevier, Amsterdam, pp. 287–437.

Stone, J.O., 2000. Air pressure and cosmogenic isotope production. *J. Geophys. Res.: Solid Earth* 105, 23753–23759.

Svendsen, J.I., Alexanderson, H., Astakhov, V.I., Demidov, I., Dowdeswell, J.A., Funder, S., Gataullin, V., Henriksen, M., Hjort, C., Houmark-Nielsen, M., Hubberten, H.W., Ingolfsson, O., Jakobsson, M., Kjaer, K.H., Larsen, E., Lorkrantz, H., Lunkka, J.P., Lysa, A., Mangerud, J., Matiouchkov, A., Murray, A., Moller, P., Niessen, F., Nikolskaya, O., Polyak, L., Saarnisto, M., Siegert, C., Siegert, M.J., Spielhagen, R.F., Stein, R., 2004. Late Quaternary ice sheet history of northern Eurasia. *Quat. Sci. Rev.* 23, 1229–1271.

Ufimtsev, G.F., Skovitina, T.M., Kulchitskiy, A.A., 1998. Rockfall-dammed lakes in the Baikal region: evidence from the past and prospects for the future. *Nat. Hazards* 18, 167–183.

von Blanckenburg, F., Belshaw, N.S., O'Nions, R.K., 1996. Separation of  $^{9}\text{Be}$  and cosmogenic  $^{10}\text{Be}$  from environmental materials and SIMS isotope dilution analysis. *Chem. Geol.* 129, 93–99.

Waitt Jr., R.B., 1980. About forty last-glacial Lake Missoula jökulhlaups through southern Washington. *J. Geol.* 88, 653–679.

Wetterich, S., Kuzmina, S., Andreev, A.A., Kienast, F., Meyer, H., Schirrmeister, L., Kuznetsova, T., Sierraalta, M., 2008. Palaeoenvironmental dynamics inferred

from late quaternary permafrost deposits on Kurungnakh island, Lena delta, Northeast Siberia, Russia. *Quat. Sci. Rev.* 27, 1523–1540.

Wiedmer, M., Montgomery, D.R., Gillespie, A.R., Greenberg, H., 2010. Late Quaternary megafloods from Glacial Lake Atna, Southcentral Alaska, U.S.A. *Quat. Res.* 73, 413–424.

Zhang, X., Prange, M., Merkel, U., Schulz, M., 2014. Instability of the Atlantic overturning circulation during Marine Isotope Stage 3. *Geophys. Res. Lett.* 41, GL060321.

Zolotarev, A.G., 1974. The Baikal-Patom Upland. In: Florensov, N.A. (Ed.), The Highlands of Cisbaikalia and Transbaikalia. Nauka, Moscow (In Russian).